

---

# Gated Domain Units for Multi-source Domain Generalization

---

Simon Föll<sup>1\*</sup> Alina Dubatovka<sup>2\*</sup> Eugen Ernst<sup>3</sup> Martin Maritsch<sup>1</sup> Patrik Okanovic<sup>2</sup>  
Gudrun Thäter<sup>3</sup> Joachim M. Buhmann<sup>2</sup> Felix Wortmann<sup>1,3</sup> Krikamol Muandet<sup>5</sup>

<sup>1</sup>Department of Management, Technology, and Economics, ETH Zurich, Switzerland

<sup>2</sup>Department of Computer Science, ETH Zurich, Switzerland

<sup>3</sup>Department of Mathematics, Karlsruhe Institute of Technology, Germany

<sup>4</sup>Institute for Technology Management, University of St. Gallen, Switzerland

<sup>5</sup>Max Planck Institute for Intelligent Systems, Germany

sfoell@ethz.ch alina.dubatovka@inf.ethz.ch euernst@kit.edu

mmaritsch@ethz.ch pokanovic@ethz.ch gudrun.thaeter@kit.edu

jbuhmann@inf.ethz.ch felix.wortmann@unisg.ch

krikamol.muandet@tuebingen.mpg.de

## Abstract

Distribution shift (DS) is a common problem that deteriorates the performance of learning machines. To overcome this problem, we postulate that real-world distributions are composed of elementary distributions that remain invariant across different domains. We call this an *invariant elementary distribution* (I.E.D.) assumption. This invariance thus enables knowledge transfer to unseen domains. To exploit this assumption in domain generalization (DG), we developed a modular neural network layer that consists of Gated Domain Units (GDUs). Each GDU learns an embedding of an individual elementary domain that allows us to encode the domain similarities during the training. During inference, the GDUs compute similarities between an observation and each of the corresponding elementary distributions which are then used to form a weighted ensemble of learning machines. Because our layer is trained with backpropagation, it can be easily integrated into existing deep learning frameworks. Our evaluation on Digits5, ECG, Camelyon17, iWildCam, and FMoW shows a significant improvement in the performance on out-of-training target domains without any access to data from the target domains. This finding supports the validity of the I.E.D. assumption in real-world data distributions.

## 1 Introduction

A fundamental assumption in machine learning is that training and test data are independently and identically distributed (I.I.D.). This assumption ensures consistency—results from statistical learning theory, meaning that the learning machine obtained from an empirical risk minimization (ERM) attains the lowest achievable risk as sample size grows [1, 2]. Unfortunately, a considerable amount of research and real-world applications in the past decades has provided a staggering evidence against this assumption [3–6] (see D’Amour *et al.* [7] for case studies). The violation of the I.I.D. assumption is usually caused by a distribution shift (DS) and can result in inconsistent learning machines [8], implying the loss of performance guarantee of machine learning models in the real world. Therefore, to tackle DS, recent work advocates for domain generalization (DG) [9–13]. This generalization to utterly unseen domains is crucial for robust deployment of the models in practical application,

---

\*These authors contributed equally.

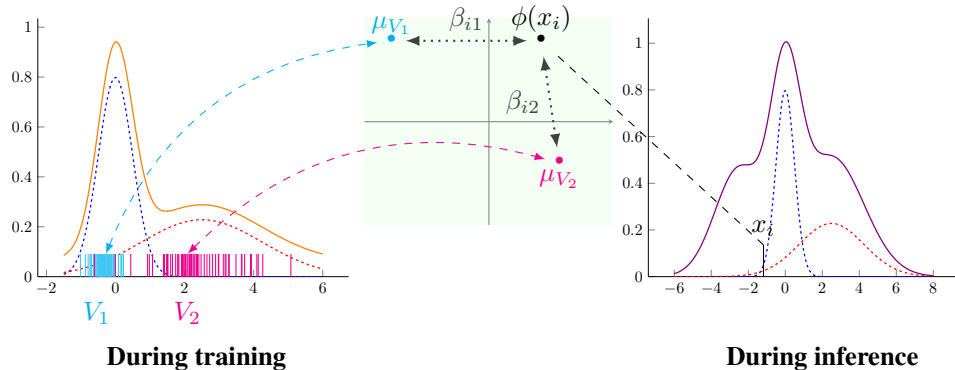


Figure 1: A visualization of an “invariant elementary distribution (I.E.D.)” assumption for domain generalization (DG): the observed data distributions (orange and violet) are composed of the same set of *unobserved* elementary distributions (blue and red) that remain invariant across different domains. Hence, the first challenge during the training phase (left panel) is to extract these elementary distributions from the observed data (orange). The unobserved elementary distributions are represented by the elementary bases  $V_1$  and  $V_2$  (cyan and pink). The second challenge during the inference phase (right panel) is to create a weighted ensemble of learning machines that utilize the similarities between the embedding of the unseen observation  $\phi(x_i)$  and the embeddings of these distributions  $\mu_{V_1}$  and  $\mu_{V_2}$  in the RKHS  $\mathcal{H}$  (green rectangle) as weights  $\beta_{i1}$  and  $\beta_{i2}$ .

especially when new, unforeseeable domains emerge after model deployment. However, the most important question that DG seeks to answer is how to identify the right *invariance* allowing for generalization.

The contribution of this work is twofold. First, we advocate that real-world distributions are composed of smaller “units” called *invariant elementary distributions* that remain invariant across different domains; see Section 2.1 for a motivating example. Second, we propose to implement this hypothesis through so-called gated domain units (GDUs). Specifically, we developed a modular neural network layer that consists of GDUs. Each GDU learns an embedding of an individual elementary domain that allows us to express the domain similarities during training. For this purpose, we adopt the theoretical framework of reproducing kernel Hilbert space (RKHS) to retrieve a geometrical representation of each distribution in the form of a kernel mean embedding (KME) without information loss [14–17]. This representation accommodates methods based on analytical geometry to measure similarities between distributions. We show that these similarity measures can be learned and utilized to improve the generalization capability of deep learning models to previously unseen domains.

The remainder of this paper is organized as follows: The theoretical framework is laid out in Section 2 with our modular DG layer implementation shown in Section 3. In Section 4, we outline related work. Our experimental evaluations are presented in Section 5. Finally, we discuss potential limitations of our approach and future work in Section 6.

## 2 Domain Generalization with Invariant Elementary Distributions

Let  $\mathcal{X}$  and  $\mathcal{Y}$  be the input and output space, with a joint distribution  $\mathbb{P}$ . In the multi-source DG setting, we are given a set of  $D$  labeled source datasets  $\{\mathcal{D}_i^s\}_{i=1}^D$  with  $\mathcal{D}_i^s \subseteq \mathcal{X} \times \mathcal{Y}$ . Each of the source datasets is assumed to be I.I.D. generated by a joint distribution  $\mathbb{P}_i^s$  with support on  $\mathcal{X} \times \mathcal{Y}$ , henceforth denoted *domain*. The set of probability measures with support on  $\mathcal{X} \times \mathcal{Y}$  is denoted by  $\mathcal{P}$ . In general, we aim to minimize the empirical risk, see Section 3.3 for details. Important notation is summarized in Table 1.

### 2.1 Invariant Elementary Distributions

A multi-source dataset  $\mathcal{D}^s$  comprises the merged individual source datasets  $\{\mathcal{D}_i^s\}_{i=1}^D$ . Similar to Mansour *et al.* [18], Albuquerque *et al.* [19], and Hoffman *et al.* [20], we assume that the distribution of the source dataset can be described as a convex combination

$\mathbb{P}^s = \sum_{i=1}^D \alpha_i^s \mathbb{P}_i^s$ , where  $\alpha^s = (\alpha_1^s, \dots, \alpha_D^s)$  is an element of the probability simplex (i.e.,  $\alpha^s \in \Delta^D := \{\alpha \in \mathbb{R}^D \mid \alpha_i \geq 0 \wedge \sum_{i=1}^D \alpha_i = 1\}$ ). In other words,  $\alpha_i$  quantifies the contribution of each individual source domain to the combined source domains.

In contrast to Mansour *et al.* [18], Hoffman *et al.* [20], and Mansour *et al.* [21], we generalize their problem descriptions: We express the distribution of each domain as a convex combination of  $K$  elementary distributions  $\{\mathbb{P}_i\}_{i=1}^K \subset \mathcal{P}$ , meaning that  $\mathbb{P}^s = \sum_{i=1}^K \alpha_i \mathbb{P}_i$ , where  $\alpha \in \Delta^K$ . We assume the elementary distributions to be invariant across the domains. The advantage is that we can find an invariant subspace at a more elementary level, as opposed to when we consider the source domains as some sort of basis for all unseen domain.

**Motivating example.** In this work, we postulate the elementary domain bases are the invariant subspaces that allow us to generalize to unseen domains. In practice, the question arises if and when elementary domains evolve. Consider the practical case of classifying the outcome of virus infections based on electronic health records collected from multiple sources such as patients, cohorts, and medical centers. Naturally, several factors determining the trajectory such as gender, pre-existing diseases, and virus mutations can change simultaneously across these sources. While, to a certain degree, these common factors remain invariant across individuals, the contribution of each of these factors may differ between individuals. In terms of the assumptions made in our work, we model each of these factors with a corresponding elementary distribution  $\mathbb{P}_i$ . For a previously unseen individual we can then determine the coefficients  $\alpha_i^s$  and therewith quantify the contribution of each factor.

## 2.2 Kernel Mean Embedding of Distributions

In this work, we leverage the KME of distributions [14, 15, 17] to discover the elementary distributions and evaluate similarities between them. Let  $\mathcal{H}$  be a reproducing kernel Hilbert space (RKHS) of real-valued functions on  $\mathcal{X}$  with a reproducing kernel  $k : \mathcal{X} \times \mathcal{X} \rightarrow \mathbb{R}$  [22]. The KME of a probability measure  $\mathbb{P} \in \mathcal{P}$  in the RKHS  $\mathcal{H}$  is defined by a mapping  $\phi(\mathbb{P}) = \mu_{\mathbb{P}} := \int_{\mathcal{X}} k(\mathbf{x}, \cdot) d\mathbb{P}(\mathbf{x})$ . We assume that the kernel  $k$  is characteristic, i.e., the mapping  $\mu_{\mathbb{P}}$  is injective [23, 24]. Theoretically, this essential assumption ensures that there is no information loss when mapping the distribution into  $\mathcal{H}$ . Given the samples  $\{x_1, \dots, x_n\}$  generated I.I.D. from  $\mathbb{P}$ ,  $\mu_{\mathbb{P}}$  can be approximated by the empirical KME  $\hat{\mu}_{\mathbb{P}} = (1/n) \sum_{i=1}^n k(x_i, \cdot) = (1/n) \sum_{i=1}^n \phi(x_i)$ . We refer non-expert readers to Muandet *et al.* [17] for a thorough review on this topic.

**Challenges.** Figure 1 depicts two challenges that come with our assumption of elementary distributions. First, since we do not have access to the samples from the hidden elementary distributions, the elementary KME cannot be estimated directly from the samples at hand. To overcome this challenge, we instead seek a proxy KME  $\mu_{V_i} := (1/N) \sum_{j=1}^N \phi(v_j^i) = (1/N) \sum_{j=1}^N k(v_j^i, \cdot)$  for each elementary KME  $\mu_{\mathbb{P}_i}$  from a domain basis  $V_i$ , where  $V_i = \{v_1^i, \dots, v_N^i\} \subseteq \mathcal{X}$  for all  $i \in \{1, \dots, M\}$ . Hence, the KME  $\mu_{V_i}$  can be interpreted as the KME of the empirical probability measure  $\hat{\mathbb{P}}_{V_i} = (1/N) \sum_{j=1}^N \delta_{v_j^i}$ . Here, we assume that  $M = K$ . The sets  $V_i$  are referred to as *elementary domain basis*. Intuitively, the elementary domain basis  $V_1, \dots, V_M$  represents each elementary distribution by a set of vectors that mimic samples generated from the corresponding distribution. In Figure 1,  $V_1$  and  $V_2$  as well as their mapping in  $\mathcal{H}$  visualize this first challenge.

The second challenge points to the objective of learning the unknown similarity between a single sample  $x_i$  and an elementary domain  $V_j$ , which we denote by  $\beta_{ij}$ . Considering the advantage of KMEs, that is to tackle this challenge from a geometrical viewpoint, we quantify similarities between KMEs. For example, in Figure 1, the similarity between  $\phi(x_i)$  and  $\mu_{V_1}$  and  $\mu_{V_2}$  could be quantified as

Table 1: Important notation

$K$	number of elementary distributions
$M$	number of elementary domain bases
$N$	number of basis vectors
$\mathbb{P}^s$	combined multi-source distribution
$\mathbb{P}_i^s$	$i$ -th single-source distribution
$\mathbb{P}_i$	$i$ -th elementary distribution
$V_i$	$i$ -th domain basis
$v_j^i$	$j$ -th vector in $V_i$
$\alpha_i^s$	coefficient for $\mathbb{P}_i^s$
$\alpha_i$	coefficient for $\mathbb{P}_i$
$\beta_{ij}$	coefficient for sample $x_i$ and $\mu_{V_j}$

their distance or angle. These similarity coefficients enable the learning machine to represent a convex combination of elementary domain-specific learning machines, commonly known as ensembles.

### 3 Domain Generalization Layer

This section aims to transfer the theoretical ideas presented in Section 2 into a deep learning framework. For the purpose of implementation, let  $x \in \mathbb{R}^{h \times w}$  denote the input data point and  $h_\xi : \mathbb{R}^{h \times w} \rightarrow \mathbb{R}^e$  the feature extractor (FE) that maps the input into a low-dimensional representation  $\tilde{x} \in \mathbb{R}^e$ . Then the prediction layer  $g_\theta : \mathbb{R}^e \rightarrow \mathcal{Y}$  infers the label  $y$ . To tackle the DG problem, we introduce a layer module called the gated domain unit (GDU). A GDU consists of three main components: (1) a similarity function  $\gamma : \mathcal{H} \times \mathcal{H} \rightarrow \mathbb{R}$  that is the same for all elementary domains, (2) an elementary basis  $V_i$  and (3) a learning machine  $f(\tilde{x}, \theta_i)$  for each elementary domain  $i \in \{1, \dots, M\}$ . The architecture of the layer proposed herein is depicted in Figure 2.

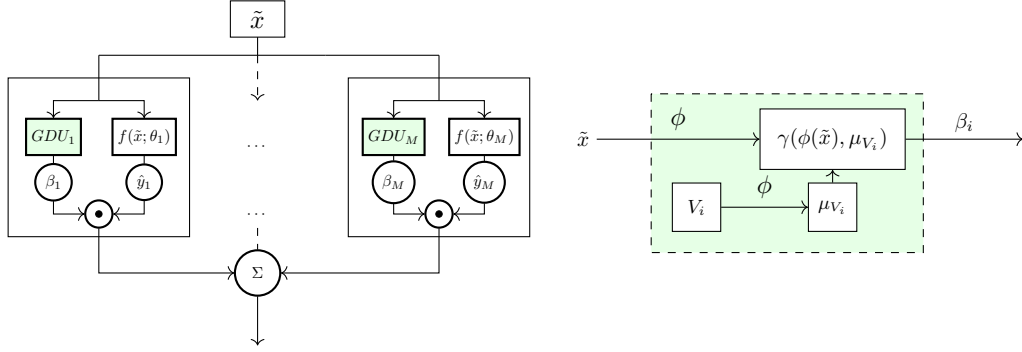


Figure 2: Visualization of the DG layer (left panel) and its main component, the GDU (right panel). The DG layer consists of several GDUs that represent the elementary distributions. During training, these GDUs learn the elementary domain bases  $V_1, \dots, V_M$  that approximate these distributions.

Essentially, the process is as follows: First, the  $j$ -th GDU takes  $\tilde{x}_i$  as an input and yields  $\beta_{ij}$  as an output. The KME of each domain basis  $V_j$  is required in order to apply  $\gamma$  to compute similarity between  $\tilde{x}_i$  and  $V_j$ . These KMEs are obtained by  $\phi(V_j) := \mu_{V_j} = (1/N) \sum_{k=1}^N \phi(v_k^j) = (1/N) \sum_{k=1}^N k(v_k^j, \cdot)$ . The GDU, therefore, has the task to allocate coefficients  $\beta_{ij}$  for each elementary domain based on a similarity function  $\gamma$ . The function  $\gamma$  outputs the  $\beta_{ij} = \gamma(\phi(\tilde{x}_i), \mu_{V_j})$  coefficients that in turn represent similarities between the KME of both, the corresponding domain basis  $V_j$  and the input  $\tilde{x}_i$ . Theoretically speaking,  $\mu_{V_j}$  and the feature mapping  $\phi(\tilde{x}_i)$  are elements of the associated RKHS  $\mathcal{H}$ , which allow us to evaluate similarities of non-linear features in a higher dimensional feature space.

Each GDU is then connected to a learning machine  $f(\tilde{x}_i, \theta_j)$  that yields an elementary domain-specific inference. The final prediction of the layer is then an ensemble of these learning machines  $g_\theta(\tilde{x}_i) = \sum_{j=1}^M \beta_{ij} f(\tilde{x}_i, \theta_j)$  where  $\theta = (\theta_1, \dots, \theta_M)$ . In Figure 2, we give an overview of how data is processed and information is stored in the GDU.

In summary, GDUs leverage the invariant elementary distribution (I.E.D.) assumption and represent our algorithmic contribution: The elementary domain basis is stored as weights in the layer. Storing information as a weight matrix (i.e., domain memory) provides the computational advantage of allowing for the use of backpropagation to learn the elementary domain basis. Hence, we avoid the dependency on problem-adaptive methods (e.g., domain-adversarial training) and metadata (e.g., domain labels).

#### 3.1 Domain Similarity Measures

For the similarity function  $\gamma$ , we consider two similarity measures  $H(\phi(x), \mu_{V_i})$ , namely the cosine similarity (CS) [25] and maximum mean discrepancy (MMD) [26, 27]. To ensure that the resulting coefficients  $\beta_i$  lie on the probability simplex, we apply the kernel softmax function [28] and interpret

its output as the similarity between an observation  $\tilde{x}$  and an elementary domain basis  $V_i$ . We get

$$\beta_i = \gamma(\phi(\tilde{x}), \mu_{V_i}) = \frac{\exp(\kappa H(\phi(\tilde{x}), \mu_{V_i}))}{\sum_{k=1}^M \exp(\kappa H(\phi(\tilde{x}), \mu_{V_k}))}, \quad (1)$$

where  $\kappa > 0$  is a positive softness parameter for the kernel softmax. Geometrically speaking, these similarities correspond to the angle and distance of two KMEs in the RKHS  $\mathcal{H}$ . The function  $\phi$  maps the observation  $\tilde{x}$  and domain basis  $V_i$  into  $\mathcal{H}$  meaning that  $\phi(x) = \mu_{\delta_x}$  is the KME of a Dirac measure  $\delta_x$  and  $\phi(V_i) = \mu_{V_i}$ .

**CS.** The CS function  $H(\phi(x), \mu_{V_i}) = \frac{\langle \phi(x), \mu_{V_i} \rangle_{\mathcal{H}}}{\|\phi(x)\|_{\mathcal{H}} \|\mu_{V_i}\|_{\mathcal{H}}}$  is used as an angle-based similarity.

**MMD.** We consider the MMD for calculating a distance-based similarity measure. The distance is then given as  $\|\phi(x) - \mu_{V_i}\|_{\mathcal{H}}$ . Subsequently, the similarity function  $H$  is the negative MMD:  $H(\phi(x), \mu_{V_i}) = -\|\phi(x) - \mu_{V_i}\|_{\mathcal{H}}$ . The intuition behind the negative MMD is to put higher weights on samples that are closer to the KME of an elementary domain basis.

### 3.2 Projection-based Generalization

For classification tasks, we introduce an alternative approach to infer the  $\beta_i$  coefficients that is based on the idea of kernel sparse coding [29, 30]. Herein the goal is to find an approximated representation of each feature mapping  $\phi(x_i)$  using the elements of a dictionary  $\{\mu_{V_j}\}_{j=1}^M$ . This approach allows us to approximate the feature mapping with these elements by  $\phi(x_i) \approx \sum_{j=1}^M \beta_{ij} \mu_{V_j}$ . In contrast to the aforementioned approaches, an elementary domain KME  $\mu_{V_j}$  does not necessarily represent the KME of an elementary distribution  $\mu_{\mathbb{P}_j}$ . Therefore, we present another approach that aims to find a set  $\{\mu_{V_j}\}_{j=1}^M$  that permits  $\mu_{\mathbb{P}_s}$  to be represented as a linear combination.

Since  $\mathbb{P}$  is assumed to be a convex combination of elementary distributions, we can find a linear combination to represent  $\mu_{\mathbb{P}_s}$  by the domain KMEs  $\mu_{V_i}$ , as long as  $\mu_{\mathbb{P}_s} \in \mathcal{H}_M := \text{span}\{\mu_{V_i} \mid i = 1, \dots, M\}$ . The RKHS  $\mathcal{H}_M$  is a subspace of the actual RKHS  $\mathcal{H}$ , which allows us to represent elements of  $\mathcal{H}$  at least approximately in the subspace  $\mathcal{H}_M$ . By keeping the  $\mathcal{H}_M$  large, we gain more representative power. To make  $\mathcal{H}_M$  as large as possible, we have to ensure its spanning elements are linearly independent or, even better, orthogonal. Orthogonal KMEs ensure two desirable properties. First, pairwise orthogonal elements in  $\mathcal{H}_M$  guarantee no redundancy. Second, having orthogonal elements allows us to make use of the orthogonal projection. This projection geometrically yields the best approximation of  $\phi(x)$  in  $\mathcal{H}_M$ . In other words, we can achieve the best possible approximation of the feature mapping by using its orthogonal components (see Proposition 3.1). The orthogonal projection is given by

$$\Pi_{\mathcal{H}_M} : \mathcal{H} \rightarrow \mathcal{H}_M, \quad \phi(x) \mapsto \sum_{i=1}^M \frac{\langle \phi(x), \mu_{V_i} \rangle_{\mathcal{H}}}{\|\mu_{V_i}\|_{\mathcal{H}}^2} \mu_{V_i}. \quad (2)$$

**Proposition 3.1.** *For a KME  $\mu_{\mathbb{P}}$  of a given mixture distribution  $\mathbb{P}$  the following holds  $\mu_{\mathbb{P}} \in \text{span}\{\mu_{V_i} \mid V_i, \forall i = 1, \dots, M\}$ , where  $\langle \mu_{V_i}, \mu_{V_j} \rangle_{\mathcal{H}} = 0, \forall i \neq j$  (i.e., the KME of the elementary domains basis are pairwise orthogonal). The value of the function  $\sum_{i=1}^M \|\mu_{\mathbb{P}} - \beta_i \mu_{V_i}\|_{\mathcal{H}_k}^2$  is minimal if the coefficients are set as  $\beta_i^* = \langle \mu_{\mathbb{P}}, \mu_{V_i} \rangle_{\mathcal{H}} / \|\mu_{V_i}\|_{\mathcal{H}}^2$ .*

The Proposition 3.1 can be used to give an approximation of  $\mu_{\mathbb{P}}$  by projecting it into  $\mathcal{H}_M$ , i.e.,  $\mu_{\mathbb{P}} \approx \sum_{i=1}^M \beta_i \mu_{V_i}$  where  $\beta_i = \langle \mu_{\mathbb{P}}, \mu_{V_i} \rangle_{\mathcal{H}} / \|\mu_{V_i}\|_{\mathcal{H}}^2$ . This best approximation property is the main advantage of our assumption in Proposition 3.1 (i.e., having orthogonal KME) and thus a potential advantage of projection-based DG. Appendix A.1 provides the proof of Proposition 3.1.

### 3.3 Model Training

For model training, we adapt the domain adaptation (DA) framework from Zhuang *et al.* [31]. Thus, our learning objective function is formalized as  $\mathcal{L}(g) + \lambda_D \Omega_D(\|g\|_{\mathcal{H}})$ . The goal of the training can be described in terms of the two components of this function. Consider a batch of training data  $\{x_1, \dots, x_b\}$ , where  $b$  is the batch size. During training, we minimize the loss function

$\mathcal{L}(g) = \frac{1}{b} \sum_{i=1}^b \mathcal{L}(\hat{y}_i, y_i) = \frac{1}{b} \sum_{i=1}^b \mathcal{L}(\sum_{j=1}^M \gamma(\phi(x_i), \mu_{V_j}) f_j(x_i), y_i)$  for an underlying task and the respective batch size. In addition, our objective is that the model learns to distinguish between different domains. Thus, the regularization  $\Omega_D$  is introduced to control the domain basis. In our case, we require the regularization  $\Omega_D$  to ensure that the KMEs of the elementary domain basis are able to represent the KMEs of the elementary domains. Therefore, we minimize the MMD between the feature mappings  $\phi(x_i)$  and the associated representation  $\sum_{j=1}^M \beta_{ij} \mu_{V_j}$ . Note that  $\beta_{ij} = \gamma(\phi(x_i), \mu_{V_j})$ . Hence, the regularization  $\Omega_D = \Omega_D^{OLS}$  is defined as  $\Omega_D^{OLS}(\|g\|_{\mathcal{H}}) = \frac{1}{b} \sum_{i=1}^b \|\phi(x_i) - \sum_{j=1}^M \beta_{ij} \mu_{V_j}\|_{\mathcal{H}}^2$  (see Appendix A.2 for details). The intuition is the objective to represent each feature mapping  $\phi(x_i)$  by the domain KMEs  $\mu_{V_i}$ . Thus, we try to minimize the MMD between the feature map and a combination of  $\mu_{V_i}$ . The minimum of the stated regularization can be interpreted as the ordinary least square-solution of a regression-problem of  $\phi(x_i)$  by the components of  $\mathcal{H}_M$ . In other words, we want to ensure that the basis  $V_i$  is contained in feature mappings  $\phi(x_i)$ .

In the particular case of projection, we want the KME of the elementary domain to be orthogonal to ensure high expressive power. For this purpose, the additional term  $\Omega_D^{\perp}$  will be introduced to ensure the desired orthogonality. Considering a kernel function with  $k(x, x) = 1$ , orthogonality would require the Gram matrix  $K_{ij} = \langle \mu_{V_i}, \mu_{V_j} \rangle_{\mathcal{H}}$  to be close to the identity matrix  $I$ . There are a variety of methods for regularizing matrices available [32, 33]. A well-known method to ensure orthogonality is the soft orthogonality (SO) regularization  $\Omega_D^{\perp} = \lambda \|K - I\|_F^2$  [33]. As pointed out by Bansal *et al.* [33], the spectral restricted isometry property (SRIP) and mutual coherence (MC) regularization can be a promising alternative for SO and thus are additionally implemented in the DG layer. Hence, in the case of projection, the regularization is given by  $\Omega_D(\|g\|_{\mathcal{H}}) = \lambda_{OLS} \Omega_D^{OLS}(\|g\|_{\mathcal{H}}) + \lambda_{ORTH} \Omega_D^{\perp}(\|g\|_{\mathcal{H}})$ ,  $\lambda_{OLS}, \lambda_{ORTH} \geq 0$ .

Lastly, sparse coding is an efficient technique to find the least possible basis to recover the data subject to a reconstruction error [34]. Several such applications yield strong performances, for example in the field of computer vision [35, 36]. Kernel sparse coding transfers the reconstruction problem of sparse coding into  $\mathcal{H}$  by using the mapping  $\phi$ , and, by applying a kernel function, the reconstruction error is quantified as the inner product [29, 30]. To ensure sparsity, we apply the  $L_1$ -norm on the coefficients  $\beta$  and add  $\Omega_D^{L_1}(\|\gamma\|) := \|\gamma(\phi(x_i), \mu_{V_j})\|_1$  to the regularization term  $\Omega_D$  with the corresponding coefficient  $\lambda_{L_1}$ . Appendix A.3 gives a visual overview of the model training.

## 4 Related Work

DG, also known as out-of-distribution (OOD) generalization, is among the hardest problems in machine learning [9, 10, 37]. In contrast, DA, which predates DG and OOD problems, deals with a slightly simpler scenario in which some data from the test distribution are available [38]. Hence, based on the available data, the task is to develop learning machines that transfer knowledge learned in a source domain specifically to the target domain. Approaches pursued in DA can be grouped primarily into (1) discrepancy-based DA [39–45] (2) adversary-based DA [38, 46–48], and (3) reconstruction-based DA [49–54]. In DA, learning the domain-invariant components requires access to unlabeled data from the target domain. Unlike problems in DA, where the observed data from the test domains can be used to find the most appropriate invariant structures [41], the lack thereof in DG calls for a postulation of invariant structure that will enable the OOD generalization.

To enable generalization to unseen domains without any access to data from them, researchers have made significant progress in the past decade and developed a broad spectrum of methodologies [9, 13, 55, 56]. For thorough review see, e.g., Zhou *et al.* [13] and Wang *et al.* [57]. Existing works can be categorized into methods based on domain-invariant representation learning [10, 12, 58], meta-learning [59, 60], data augmentation [61], to name a few. Another recent stream of research from a causal perspective includes invariant risk minimization [37], invariant causal prediction [62], and causal representation learning [63]. The overall motivation here is to learn the representation that is robust to domain-specific spurious correlations. In other words, it is postulated that ‘‘causal’’ features are the right kind of invariance that will enable OOD generalization. Despite the successful applications, DG remains a challenging research gap.

We differentiate our work from existing ones as follow. First, we postulate the existence of domain-invariant structure at the distributional level rather than at the data representation, which is a common assumption in DG. This is motivated by theoretical results [20, 21], stating that a distribution-weighted

combination of source hypotheses represents the ideal hypothesis. Furthermore, our distributional assumption, as we argued in Section 2, generalizes previous work that proposes to use domain-specific knowledge to tackle the problem of DG from a more elementary setting. For example, approaches such as Piratla *et al.* [64] and Monteiro *et al.* [65] can be compared to our GDUs as domain-specific predictors, in the special case, where each elementary domain represents a single source domain. However, GDUs do not assume the existence of a single common classifier for all the domains, providing a combination of multiple common classifiers shared between different source domains.

Second, we incorporate the I.E.D. assumption directly into the design of our model architectures as shown in Figure 2. Designing effective model architectures for DG has been largely neglected [61, Sec. 4.1]. Third, we do not assume access to the domain labels, which can be difficult to obtain in practice [66]. As DG methods that can deal with the absence of domain labels (e.g., [67–69]) are still scarce [61, Sec. 4.2], we provide an easy-to-apply method to achieve OOD generalization: `model.add(DGLayer())` in TensorFlow.

## 5 Experiments

The goal of our experiments is to validate the proposed I.E.D. assumption and the working principle of the GDUs. Further, we conduct a benchmark experiment based on real-world datasets for DG. We distinguish two modes of training the DG layer: fine tuning (FT), where we extract features using a pre-trained model, and end-to-end training (E2E), where the FE and the DG layer are jointly trained.<sup>2</sup>

### 5.1 Digits Experiment

We use five publicly available digits image datasets, namely MNIST [70], MNIST-M [71], SVHN [72], USPS, and Synthetic Digits (SYN) [71]. For this experiment, we follow the experimental setup of Zhao *et al.* [3], Peng *et al.* [73], Feng *et al.* [74], and Zhang *et al.* [75]. The task is to classify digits between zero and nine. Each of these datasets is considered an out-of-training target domain which is inaccessible during training, and the remaining four are the source domains. Details are given in Appendix A.4.1. In Table 2 summarizes the classification results for this experiment. Our DG layer noticeably improves mean accuracy and decreases the standard deviation in comparison to the ERM and ERM ensemble baselines, making the results more stable across the ten iterations reported.

Table 2: Results Digits experiment. All experiments were repeated ten times and the mean (standard deviation) accuracy is reported. Best results according to the mean accuracy are highlighted in **bold**.

		MNIST	MNIST-M	SVHN	USPS	SYN
<b>ERM</b>	Single	97.98 (0.34)	63.00 (3.20)	70.18 (2.74)	93.70 (1.74)	83.62 (1.47)
	Ensemble	98.21 (0.39)	62.87 (1.50)	72.01 (3.59)	95.16 (0.89)	83.80 (1.22)
<b>FT</b>	CS	98.53 (0.16)	68.55 (0.80)	78.90 (1.41)	95.83 (0.50)	88.39 (0.82)
	MMD	98.60 (0.08)	68.62 (0.70)	79.20 (2.01)	<b>96.24 (0.71)</b>	88.27 (0.41)
	PROJECTION	98.57 (0.17)	68.56 (0.91)	79.34 (0.72)	96.24 (0.71)	88.58 (0.53)
<b>E2E</b>	CS	98.62 (0.19)	<b>69.25 (0.61)</b>	<b>79.42 (1.27)</b>	96.17 (0.52)	87.92 (0.84)
	MMD	98.58 (0.16)	69.04 (0.83)	79.20 (0.90)	96.00 (0.44)	88.18 (0.86)
	PROJECTION	<b>98.67 (0.12)</b>	68.67 (0.98)	78.56 (1.68)	96.24 (0.77)	<b>88.77 (0.48)</b>

### 5.2 Ablation Study

We chose the digits dataset to analyze each component of our DG layer. We (a) discuss heuristics for choosing  $\sigma$  and  $M$  (Appendix A.4.2), (b) vary  $M$ ,  $N$  on Figure 8, and the strength of the regularization terms on Figure 6, Figure 5, and Figure 7 to assess the sensitivity of the DG layer to the choice of hyper-parameters (Appendix A.4.3), (c) visualize the output of the FE (Figure 4), and (d) interpret the learned elementary domains (Appendix A.4.4). For (a), we cluster the output of the FE using k-means algorithm with different number of clusters  $K$  and set the number of elementary domains

<sup>2</sup>All source code is made available on GitHub <https://github.com/im-ethz/pub-gdu4dg>.

$M$  to the  $K^*$  yielding the best clustering. For  $\sigma$ , we resort to the median heuristics [17]. Further, our ablation study (b) reveals stable results across different sets of hyper-parameters. While the layer is not sensitive to the choice of regularization strength, we recommend not to omit the regularization completely although the computational expenses decrease without the orthogonal regularization. As an illustration in (c), we project the output of the FE trained with a dense layer (ERM) and with the DG layer by t-SNE (t-distributed stochastic neighbor embedding). The DG-trained FE yields more concentrated and bounded clusters in comparison to the one trained by ERM. For (d), the MMD heatmap and t-SNE embeddings of the learned elementary and source domains on Figure 10 indicate that the DG captures distributional structures in the dataset.

### 5.3 ECG Experiment

The PhysioNet/Computing in Cardiology Challenge 2020 [76–78] aims at identifying clinical diagnoses from 12-lead ECG recordings coming from 6 different databases. This publicly available pooled dataset contains 43,101 recordings sampled with various sampling frequencies and lengths. Each recording is labeled as having one or more of 24 cardiac abnormalities and, hence, the task is to perform a multi-label binary classification. For our experiment, we iterate over the databases, taking one at a time as the test domain while utilizing the remaining 5 databases for training.

The performance was measured according to the original PhysioNet challenge score which is defined as a generalized intersection-over-union score where partial credit is assigned to misdiagnoses that result in similar treatments or outcomes. The score is then adjusted for a solution which always selects the normal/majority class and normalized for the perfect solution. Therefore, the score can have negative values and a best possible score of 1.

Table 3 reports results for the ECG experiments. For this kind of real-world time-series data we observe an improvement in mean score and reduction in standard deviation over the ERM and ERM ensemble baselines across all generalization tasks. We attribute poorer performance for the *PTB* dataset to the fact that it contains considerably longer recordings than other datasets (except for *INCART* which, however, contains only 75 samples) and higher sampling rate (1000Hz vs 500Hz and 257Hz). The negative challenge score for the *PTB-XL* dataset is due to the presence of previously unobserved labels in other datasets as well as a considerably smaller amount of data for training since the *PTB-XL* dataset comprises the majority of all samples (21,837 out of 43,101). Appendix A.4.5 provides details for this experiment.

Table 3: Results ECG experiment. All experiments were repeated five times and the mean (standard deviation) challenge metric is reported. Higher is better. Best overall results according to the mean challenge metric are highlighted in **bold**.

		CPSC	CPSC-EXTRA	INCART	PTB	PTB-XL	G12EC
<b>ERM</b>	Single	0.0840 (0.0220)	0.2715 (0.0270)	0.2290 (0.0059)	-8.8206 (0.3908)	-0.3373 (0.0403)	0.2011 (0.0015)
	Ensemble	0.1699 (0.0346)	0.2488 (0.0079)	0.2456 (0.0109)	-8.9115 (0.1023)	-0.4136 (0.0780)	0.2079 (0.0161)
<b>FT</b>	CS	0.1830 (0.0061)	0.2950 (0.0035)	0.1595 (0.0313)	-8.8802 (0.1069)	-0.1932 (0.0168)	0.1853 (0.0036)
	MMD	0.1877 (0.0077)	0.3011 (0.0035)	0.2100 (0.0413)	-8.8082 (0.1458)	-0.1567 (0.0211)	0.1919 (0.0036)
	PROJECTION	<b>0.1941 (0.0050)</b>	<b>0.3135 (0.0015)</b>	-0.1041 (0.0015)	-8.8817 (0.0478)	-0.2166 (0.0191)	0.2409 (0.0042)
<b>E2E</b>	CS	0.1067 (0.0170)	0.2866 (0.0146)	<b>0.2539 (0.0289)</b>	-9.2947 (0.3004)	-0.1651 (0.0494)	0.1927 (0.0080)
	MMD	0.1034 (0.0143)	0.2834 (0.0228)	0.2398 (0.0257)	-9.0600 (0.3100)	-0.1433 (0.0293)	0.1925 (0.0067)
	PROJECTION	0.1411 (0.0269)	0.2962 (0.0065)	-0.1467 (0.0513)	<b>-8.5904 (0.3310)</b>	<b>-0.0178 (0.0291)</b>	<b>0.2947 (0.0117)</b>

### 5.4 WILDS Benchmark

To challenge the I.E.D. assumption and the generalization capabilities of the DG layer, we use WILDS, a curated set of real-world experiments for benchmarking DG methods [79]. We consider the following four datasets: *Camelyon17*, *RxRx1*, *iWildCam*, and *FMoW*, which represent the task of real-world DG. Appendix A.4.6 provides details on the datasets and experiments.

Following the WILDS benchmarking procedure [79], we compare our proposed DG layer to the following baselines. First, empirical risk minimization (ERM), which minimizes the average training



loss over the pooled dataset. Second, a group of DG algorithms provided by the WILDS benchmark, namely, Coral, Fish, IRM, and DRO. The Coral algorithm introduces a penalty for differences in means and covariances of the domains feature distributions. The Fish algorithm achieves DG by approximating an inter-domain gradient matching objective, i.e., maximizing the inner product between gradients from different domains [80]. Conceptually, Fish learns feature representations that are invariant across domains. Invariant risk minimization (IRM) introduces a penalty for feature distributions with different optimal classifiers for each domain [37]. The idea is to enable OOD generalization by learning domain-invariant causal predictors. Lastly, group distributionally robust optimization (DRO) explicitly minimizes the training loss on the worst-case domain [81, 82].

We present our benchmarking results in Table 4. When reproducing the ERM results, we noticed two deviations from the original results presented in Koh *et al.* [79]. For *Camelyon17*, we achieved a better accuracy with a simpler FE. For the remaining datasets, our ERM achieved lower performances although we used the same specifications made in Koh *et al.* [79]. Hence, we report our reproduced ERM results as a baseline for comparison. As shown by Koh *et al.* [79], ERM remains one of the strongest baselines in real-world DG problems. Our method consistently increases the mean performance and decreases the standard deviation in comparison to ERM. For *RxRx1*, however, our method does not outperform the baseline. In contrast to our digits and ECG experiments, the WILDS benchmarking requires deeper FE such as ResNet-50 or DenseNet-121. We discuss the scalability of our DG Layer in the Appendix A.4.7.

Table 4: Results on WILDS benchmarking tasks. We compute the metrics following Koh *et al.* [79] and report the mean (standard deviation) across ten runs for *Camelyon17* and three runs for the remaining. Best performances in comparison with our ERM are highlighted in **bold**.

	CAMELYON17	RxRx1	IWILDCAM		FMoW		
	AVG ACC	AVG ACC	AVG ACC	MACRO F1	AVG ACC	AVG WORST-REGION ACC	
<b>ERM</b>	77.8 (12.7)	<b>26.9 (0.0)</b>	67.0 (3.9)	16.7 (0.6)	46.1 (1.5)	24.5 (0.9)	
CS	<b>79.2 (10.1)</b>	25.3 (0.1)	68.9 (1.6)	16.5 (0.4)	51.7 (0.2)	30.4 (0.3)	
<b>FT</b>	MMD	78.5 (11.9)	25.3 (0.1)	70.3 (3.2)	16.9 (0.4)	<b>51.9 (0.7)</b>	<b>31.8 (0.9)</b>
PROJECTION	78.6 (11.9)	25.1 (0.3)	<b>71.2 (2.6)</b>	<b>17.2 (0.6)</b>	51.5 (0.2)	30.2 (1.1)	
CS	76.7 (11.4)	16.3 (0.2)	65.6 (1.8)	15.6 (1.0)	47.0 (0.6)	28.2 (0.7)	
<b>E2E</b>	MMD	75.5 (12.8)	16.2 (0.1)	67.5 (2.6)	15.7 (0.6)	47.6 (2.1)	27.1 (2.7)
PROJECTION	76.7 (6.3)	13.9 (0.1)	67.4 (0.2)	15.4 (1.1)	47.4 (0.9)	28.6 (1.6)	
<i>Results reported by WILDS [79]</i>							
<b>ERM</b>	70.3 (6.4)	29.9 (0.4)	71.6 (2.5)	31.0 (1.3)	53.0 (0.6)	33.7 (1.5)	
<b>CORAL</b>	59.3 (7.7)	28.4 (0.3)	73.3 (4.3)	32.8 (0.1)	50.5 (0.4)	31.7 (1.2)	
<b>FISH</b>	74.7 (7.1)	–	64.7 (2.6)	22.0 (1.8)	51.8 (0.3)	34.6 (0.2)	
<b>IRM</b>	64.2 (8.1)	8.2 (1.1)	59.8 (3.7)	15.1 (4.9)	50.8 (0.1)	30.0 (1.4)	
<b>GROUP DRO</b>	68.4 (7.3)	23.0 (0.3)	72.7 (2.0)	23.9 (2.1)	52.1 (0.5)	30.8 (0.8)	

## 6 Conclusion and Discussions

We introduced the I.E.D. assumption, postulating that real-world distributions are composed of elementary distributions that remain invariant across different domains. This invariance thus enables knowledge transfer to unseen domains. Empirical results based on real-world data support the validity of the I.E.D. assumption. In *Camelyon17*, for example, we would expect similar subpopulations across hospitals, which may constitute elementary domains. In contrast, when the number of elementary domains become excessively large, as we suspect in the *RxRx1* dataset, representing them becomes difficult. Further, we presented a modular neural network layer consisting of Gated Domain Units (GDUs) that leverage the I.E.D. assumption. Our GDUs can substantially improve the downstream performance of learning machines in real-world DG tasks.

We expect the I.E.D. assumption and GDUs to be adapted yielding novel applications that tackle DG. For example, adaptively increasing the number of elementary domains during learning until their distributional variance, as a measure of their heterogeneity, reaches a plateau.

**Limitations.** A major limitation of our I.E.D. assumption is to provide theoretical evidence that this assumption holds in practice. We aim to expand the scope of the theoretical understanding of the I.E.D. assumption and the GDUs. In addition, the particular theoretical setting of Albuquerque *et al.* [19] (i.e., each elementary domain represents a source domain) seems promising to extend their generalization guarantee to cases where our I.E.D. assumption holds. Second, our GDU layer induces additional computational overhead due to the regularization and model size that increases as a function of the number of elementary domains. Noteworthy, our improvement is achieved with a relatively small number of elementary domains indicating that the increased complexity is not a coercive consequence of applying the DG layer. Also, the results achieved are not a consequence of increased complexity, as the ensemble baseline shows.

**Societal Impact.** On a downside, our method may be used to target unknown populations or ethnicities with potentially harmful applications. For example, consider facial recognition in public spaces, where our approach can improve model performance for yet unseen populations, thereby allowing for more extensive surveillance as a whole. However, this impact is a general result of DG.

## References

1. Vapnik, V. N. *Statistical Learning Theory* (Wiley-Interscience, 1998).
2. Schölkopf, B. Causality for Machine Learning. *arXiv*, 1–20. arXiv: 1911.10500 (2019).
3. Zhao, H. *et al.* *Adversarial Multiple Source Domain Adaptation in Advances in Neural Information Processing Systems* (eds Bengio, S. *et al.*) **31** (Curran Associates, Inc., 2018).
4. Zhao, S. *et al.* A Review of Single-Source Deep Unsupervised Visual Domain Adaptation. *IEEE Transactions on Neural Networks and Learning Systems*, 1–21 (2020).
5. Ren, J. *et al.* *Likelihood Ratios for Out-of-Distribution Detection in Advances in Neural Information Processing Systems* (eds Wallach, H. *et al.*) **32** (Curran Associates, Inc., 2019).
6. Taori, R. *et al.* Measuring Robustness to Natural Distribution Shifts in Image Classification. *arXiv:2007.00644*. arXiv: 2007.00644 (2020).
7. D’Amour, A. *et al.* Underspecification Presents Challenges for Credibility in Modern Machine Learning. arXiv: 2011.03395 (2020).
8. Sugiyama, M. & Kawanabe, M. *Machine Learning in Non-Stationary Environments: Introduction to Covariate Shift Adaptation* (The MIT Press, 2012).
9. Blanchard, G., Lee, G. & Scott, C. *Generalizing from Several Related Classification Tasks to a New Unlabeled Sample in Advances in Neural Information Processing Systems* **24** (2011), 9.
10. Muandet, K., Balduzzi, D. & Schölkopf, B. *Domain Generalization via Invariant Feature Representation in Proceedings of the 30th International Conference on Machine Learning* (eds Dasgupta, S. & McAllester, D.) (PMLR, 2013), 10–18.
11. Li, D., Yang, Y., Song, Y.-Z. & Hospedales, T. M. *Deeper, Broader and Artier Domain Generalization in 2017 IEEE International Conference on Computer Vision (ICCV)* (IEEE, Venice, 2017), 5543–5551.
12. Li, H., Pan, S. J., Wang, S. & Kot, A. C. *Domain Generalization with Adversarial Feature Learning in 2018 IEEE/CVF Conference on Computer Vision and Pattern Recognition* (IEEE, Salt Lake City, UT, 2018), 5400–5409.
13. Zhou, K., Liu, Z., Qiao, Y., Xiang, T. & Loy, C. C. Domain Generalization: A Survey. *ArXiv210302503 Cs*. arXiv: 2103.02503 [cs] (2021).
14. Berlinet, A. & Thomas-Agnan, C. *Reproducing Kernel Hilbert Spaces in Probability and Statistics* (Kluwer Academic Publishers, 2004).
15. Smola, A. J., Gretton, A., Song, L. & Schölkopf, B. *A Hilbert space embedding for distributions in Proceedings of the 18th International Conference on Algorithmic Learning Theory (ALT)* (Springer-Verlag, 2007), 13–31.
16. Sriperumbudur, B. K., Arthur, G., Kenji, F., Schölkopf, B. & Lanckriet, G. R. Hilbert Space Embeddings and Metrics on Probability Measures. *J. Mach. Learn. Res.* **11**, 1517–1561 (2010).
17. Muandet, K., Fukumizu, K., Sriperumbudur, B. & Schölkopf, B. Kernel Mean Embedding of Distributions: A Review and Beyond. *Foundations and Trends in Machine Learning* **10**, 1–141 (2017).

18. Mansour, Y., Mohri, M. & Rostamizadeh, A. Multiple Source Adaptation and the Renyi Divergence. *Proc. 25th Conf. Uncertain. Artif. Intell. UAI 2009*, 367–374. arXiv: 1205.2628 (2012).
19. Albuquerque, I., Monteiro, J., Darvishi, M., Falk, T. H. & Mitliagkas, I. Generalizing to Unseen Domains via Distribution Matching. *ArXiv Prepr. ArXiv191100804*. arXiv: 1911.00804 (2019).
20. Hoffman, J., Mohri, M. & Zhang, N. *Algorithms and Theory for Multiple-Source Adaptation in Advances in Neural Information Processing Systems* (eds Bengio, S. et al.) **31** (Curran Associates, Inc., 2018).
21. Mansour, Y., Mohri, M. & Rostamizadeh, A. *Domain Adaptation with Multiple Sources in Advances in Neural Information Processing Systems* (eds Koller, D., Schuurmans, D., Bengio, Y. & Bottou, L.) **21** (Curran Associates, Inc., 2009).
22. Schölkopf, B., Herbrich, R. & Smola, A. J. in *Computational Learning Theory* (eds Goos, G., Hartmanis, J., van Leeuwen, J., Helmbold, D. & Williamson, B.) 416–426 (Springer Berlin Heidelberg, Berlin, Heidelberg, 2001).
23. Fukumizu, K., Bach, F. R. & Jordan, M. I. Dimensionality Reduction for Supervised Learning with Reproducing Kernel Hilbert Spaces. *Journal of Machine Learning Research* **5**, 73–99 (2004).
24. Sriperumbudur, B., Gretton, A., Fukumizu, K., Lanckriet, G. & Schölkopf, B. *Injective Hilbert space embeddings of probability measures in The 21st Annual Conference on Learning Theory (COLT)* (Omnipress, 2008), 111–122.
25. Kim, G., Okuno, A., Fukui, K. & Shimodaira, H. *Representation Learning with Weighted Inner Product for Universal Approximation of General Similarities in Proceedings of the Twenty-Eighth International Joint Conference on Artificial Intelligence, IJCAI-19* (International Joint Conferences on Artificial Intelligence Organization, 2019), 5031–5038.
26. Borgwardt, K. M. et al. Integrating Structured Biological Data by Kernel Maximum Mean Discrepancy. *Bioinformatics* **22**, e49–e57 (2006).
27. Gretton, A., Borgwardt, K. M., Rasch, M. J., Schölkopf, B. & Smola, A. A Kernel Two-Sample Test. *J. Mach. Learn. Res.* **13**, 723–773 (2012).
28. Gao, Y., Herold, C., Wang, W. & Ney, H. Exploring Kernel Functions in the Softmax Layer for Contextual Word Classification. *arXiv*. arXiv: 1910.12554 (2019).
29. Gao, S., Tsang, I. W.-H. & Chia, L.-T. *Kernel Sparse Representation for Image Classification and Face Recognition in Computer Vision – ECCV 2010* (eds Daniilidis, K., Maragos, P. & Paragios, N.) (Springer Berlin Heidelberg, Berlin, Heidelberg, 2010), 1–14.
30. Gao, S., Tsang, I. W. & Chia, L. Sparse Representation With Kernels. *IEEE Transactions on Image Processing* **22**, 423–434 (2013).
31. Zhuang, F. et al. A Comprehensive Survey on Transfer Learning. *Proceedings of the IEEE* **109**, 43–76 (2021).
32. Xie, P., Póczos, B. & Xing, E. *Near-Orthogonality Regularization in Kernel Methods in UAI* (2017).
33. Bansal, N., Chen, X. & Wang, Z. *Can We Gain More from Orthogonality Regularizations in Training Deep Networks?* in *Advances in Neural Information Processing Systems* (eds Bengio, S. et al.) **31** (Curran Associates, Inc., 2018).
34. Olshausen, B. A. & Field, D. J. Sparse Coding with an Overcomplete Basis Set: A Strategy Employed by V1? *Vision Res.* **37**, 3311–3325 (1997).
35. Lee, H., Battle, A., Raina, R. & Ng, A. *Efficient Sparse Coding Algorithms in Advances in Neural Information Processing Systems* (eds Schölkopf, B., Platt, J. & Hoffman, T.) **19** (MIT Press, 2007).
36. Yang, J., Yu, K., Gong, Y. & Huang, T. *Linear Spatial Pyramid Matching Using Sparse Coding for Image Classification in 2009 IEEE Conference on Computer Vision and Pattern Recognition* (2009), 1794–1801.
37. Arjovsky, M., Bottou, L., Gulrajani, I. & Lopez-Paz, D. Invariant Risk Minimization. arxiv:1907.02893 (2019).
38. Ganin, Y. et al. Domain-Adversarial Training of Neural Networks. *Adv. Comput. Vis. Pattern Recognit.* **17**, 189–209. arXiv: 1505.07818 (2015).
39. Sun, B., Feng, J. & Saenko, K. Return of Frustratingly Easy Domain Adaptation. *30th AAAI Conf. Artif. Intell. AAAI 2016*, 2058–2065. arXiv: 1511.05547 (2016).

40. Peng, X. & Saenko, K. *Synthetic to Real Adaptation with Generative Correlation Alignment Networks* in *2018 IEEE Winter Conference on Applications of Computer Vision (WACV)* (2018), 1982–1991.
41. Ben-David, S. *et al.* A Theory of Learning from Different Domains. *Mach. Learn.* **79**, 151–175 (2010).
42. Fang, T., Lu, N., Niu, G. & Sugiyama, M. *Rethinking Importance Weighting for Deep Learning under Distribution Shift* in *Advances in Neural Information Processing Systems* (eds Larochelle, H., Ranzato, M., Hadsell, R., Balcan, M. F. & Lin, H.) **33** (Curran Associates, Inc., 2020), 11996–12007.
43. Tzeng, E., Hoffman, J., Zhang, N., Saenko, K. & Darrell, T. Deep Domain Confusion: Maximizing for Domain Invariance. arXiv: 1412.3474 (2014).
44. Long, M., Cao, Y., Wang, J. & Jordan, M. I. Learning Transferable Features with Deep Adaptation Networks. *32nd Int. Conf. Mach. Learn. ICML 2015* **1**, 97–105. arXiv: 1502.02791 (2015).
45. Baktashmotlagh, M., Harandi, M. & Salzmann, M. Distribution-Matching Embedding for Visual Domain Adaptation. *J. Mach. Learn. Res.* **17**, 1–30 (2016).
46. Tzeng, E., Hoffman, J., Saenko, K. & Darrell, T. *Adversarial Discriminative Domain Adaptation* in *2017 IEEE Conference on Computer Vision and Pattern Recognition (CVPR)* (2017), 2962–2971.
47. Liu, M.-Y. & Tuzel, O. *Coupled Generative Adversarial Networks* in *Advances in Neural Information Processing Systems* (eds Lee, D., Sugiyama, M., Luxburg, U., Guyon, I. & Garnett, R.) **29** (Curran Associates, Inc., 2016).
48. Long, M., CAO, Z., Wang, J. & Jordan, M. I. *Conditional Adversarial Domain Adaptation* in *Advances in Neural Information Processing Systems* (eds Bengio, S. *et al.*) **31** (Curran Associates, Inc., 2018).
49. Bousmalis, K., Trigeorgis, G., Silberman, N., Krishnan, D. & Erhan, D. *Domain Separation Networks* in *Advances in Neural Information Processing Systems* (eds Lee, D., Sugiyama, M., Luxburg, U., Guyon, I. & Garnett, R.) **29** (Curran Associates, Inc., 2016).
50. Hoffman, J. *et al.* CyCADA: Cycle-Consistent Adversarial Domain Adaptation in *Proceedings of the 35th International Conference on Machine Learning* (eds Dy, J. & Krause, A.) **80** (PMLR, Stockholm, Sweden, 2018), 1989–1998.
51. Kim, T., Cha, M., Kim, H., Lee, J. K. & Kim, J. *Learning to Discover Cross-Domain Relations with Generative Adversarial Networks* in *Proceedings of the 34th International Conference on Machine Learning* (eds Precup, D. & Teh, Y. W.) **70** (PMLR, International Convention Centre, Sydney, Australia, 2017), 1857–1865.
52. Yi, Z., Zhang, H., Tan, P. & Gong, M. *DualGAN: Unsupervised Dual Learning for Image-to-Image Translation* in *2017 IEEE International Conference on Computer Vision (ICCV)* (2017), 2868–2876.
53. Zhu, J., Park, T., Isola, P. & Efros, A. A. *Unpaired Image-to-Image Translation Using Cycle-Consistent Adversarial Networks* in *2017 IEEE International Conference on Computer Vision (ICCV)* (2017), 2242–2251.
54. Ghifary, M., Bastiaan Kleijn, W. & Zhang, M. Domain Adaptive Neural Networks for Object Recognition. *Lect. Notes Comput. Sci. Subser. Lect. Notes Artif. Intell. Lect. Notes Bioinforma.* **8862**, 898–904. arXiv: 1409.6041 (2014).
55. Zhou, K., Yang, Y., Qiao, Y. & Xiang, T. *Domain Generalization with MixStyle* in *International Conference on Learning Representations* (2021), 15.
56. Li, Y., Yang, Y., Zhou, W. & Hospedales, T. *Feature-Critic Networks for Heterogeneous Domain Generalization* in *Proceedings of the 36th International Conference on Machine Learning* (eds Chaudhuri, K. & Salakhutdinov, R.) **97** (PMLR, 2019), 3915–3924.
57. Wang, J., Lan, C., Liu, C., Ouyang, Y. & Qin, T. Generalizing to Unseen Domains: A Survey on Domain Generalization. *CoRR* **abs/2103.03097** (2021).
58. Li, Y. *et al.* *Deep Domain Generalization via Conditional Invariant Adversarial Networks* in *Computer Vision – ECCV 2018* (eds Ferrari, V., Hebert, M., Sminchisescu, C. & Weiss, Y.) (Springer International Publishing, Cham, 2018), 647–663.
59. Li, D., Yang, Y., Song, Y.-Z. & Hospedales, T. M. *Learning to Generalize: Meta-learning for Domain Generalization* in *AAAI* (2018).

60. Balaji, Y., Sankaranarayanan, S. & Chellappa, R. *MetaReg: Towards Domain Generalization Using Meta-Regularization* in *Advances in Neural Information Processing Systems* (eds Bengio, S. et al.) **31** (Curran Associates, Inc., 2018).
61. Zhou, K., Yang, Y., Hospedales, T. & Xiang, T. Deep Domain-Adversarial Image Generation for Domain Generalisation. *AAAI* **34**, 13025–13032 (2020).
62. Peters, J., BÄEhlmann, P. & Meinshausen, N. Causal inference by using invariant prediction: identification and confidence intervals. *Journal of the Royal Statistical Society: Series B (Statistical Methodology)* **78**, 947–1012 (2016).
63. Schölkopf, B. et al. Toward Causal Representation Learning. *Proceedings of the IEEE* **109**, 612–634 (2021).
64. Piratla, V., Netrapalli, P. & Sarawagi, S. *Efficient Domain Generalization via Common-Specific Low-Rank Decomposition* in *Proceedings of the 37th International Conference on Machine Learning* (eds III, H. D. & Singh, A.) **119** (PMLR, Proceedings of Machine Learning Research, 2020), 7728–7738.
65. Monteiro, J., Gibert, X., Feng, J., Dumoulin, V. & Lee, D.-S. *Domain Conditional Predictors for Domain Adaptation* in *NeurIPS 2020 Workshop on Pre-registration in Machine Learning* (eds Bertinetto, L., Henriques, J. F., Albanie, S., Paganini, M. & Varol, G.) **148** (PMLR, Proceedings of Machine Learning Research, 2021), 193–220.
66. Niu, L., Li, W., Xu, D. & Cai, J. Visual Recognition by Learning From Web Data via Weakly Supervised Domain Generalization. *IEEE Transactions on Neural Networks and Learning Systems* **28**, 1985–1999 (2017).
67. Huang, Z., Wang, H., Xing, E. P. & Huang, D. *Self-Challenging Improves Cross-Domain Generalization in Computer Vision – ECCV 2020* (eds Vedaldi, A., Bischof, H., Brox, T. & Frahm, J.-M.) (Springer International Publishing, Cham, 2020), 124–140.
68. Carlucci, F. M., D’Innocente, A., Bucci, S., Caputo, B. & Tommasi, T. *Domain Generalization by Solving Jigsaw Puzzles* in *2019 IEEE/CVF Conference on Computer Vision and Pattern Recognition (CVPR)* (IEEE, Long Beach, CA, USA, 2019), 2224–2233.
69. Li, W., Xu, Z., Xu, D., Dai, D. & Gool, L. V. Domain Generalization and Adaptation Using Low Rank Exemplar SVMs. *IEEE Transactions on Pattern Analysis and Machine Intelligence* **40**, 1114–1127 (2018).
70. Lecun, Y., Bottou, L., Bengio, Y. & Haffner, P. Gradient-Based Learning Applied to Document Recognition. *Proceedings of the IEEE* **86**, 2278–2324 (1998).
71. Ganin, Y. & Lempitsky, V. *Unsupervised Domain Adaptation by Backpropagation* in *Proceedings of the 32nd International Conference on Machine Learning* (eds Bach, F. & Blei, D.) **37** (PMLR, 2015), 1180–1189.
72. Netzer, Y. et al. *Reading Digits in Natural Images with Unsupervised Feature Learning* in *NIPS Workshop on Deep Learning and Unsupervised Feature Learning 2011* (2011).
73. Peng, X. et al. *Moment Matching for Multi-Source Domain Adaptation* in *2019 IEEE/CVF International Conference on Computer Vision (ICCV)* (2019), 1406–1415.
74. Feng, H.-Z. et al. *KD3A: Unsupervised Multi-Source Decentralized Domain Adaptation via Knowledge Distillation*. *ArXiv Prepr. ArXiv201109757*. arXiv: 2011.09757 (2020).
75. Zhang, K. et al. *Domain Adaptation as a Problem of Inference on Graphical Models* in *Advances in Neural Information Processing Systems* (eds Larochelle, H., Ranzato, M., Hadsell, R., Balcan, M. F. & Lin, H.) **33** (Curran Associates, Inc., 2020), 4965–4976.
76. Perez Alday, E. A. et al. Classification of 12-lead ECGs: the PhysioNet/Computing in Cardiology Challenge 2020. *Physiol Meas* **41**, 124003 (2021).
77. Goldberger, A. L. et al. PhysioBank, PhysioToolkit, and PhysioNet: Components of a New Research Resource for Complex Physiologic Signals. *Circulation* **101**. Circulation Electronic Pages: <http://circ.ahajournals.org/content/101/23/e215.full> PMID:1085218; e215–e220 (2000).
78. Perez Alday, E. A. et al. Classification of 12-lead ECGs: the PhysioNet/Computing in Cardiology Challenge 2020 (version 1.0.1). *PhysioNet* (2020).
79. Koh, P. W. et al. *WILDS: A Benchmark of in-the-Wild Distribution Shifts* 2021. arXiv: 2012.07421 [cs.LG].
80. Shi, Y. et al. Gradient Matching for Domain Generalization. *arXiv* (2021).

81. Sagawa, S., Koh, P. W., Hashimoto, T. B. & Liang, P. *Distributionally Robust Neural Networks for Group Shifts: On the Importance of Regularization for Worst-Case Generalization in International Conference on Learning Representations 2020* (2020), 19.
82. Hu, W., Niu, G., Sato, I. & Sugiyama, M. *Does Distributionally Robust Supervised Learning Give Robust Classifiers?* in *Proceedings of the 35th International Conference on Machine Learning* (eds Dy, J. & Krause, A.) **80** (PMLR, 2018), 2029–2037.
83. Zhou, K., Yang, Y., Hospedales, T. & Xiang, T. *Learning to Generate Novel Domains for Domain Generalization 2021*. arXiv: 2007.03304 [cs].
84. Li, P. *et al.* *A Simple Feature Augmentation for Domain Generalization in Proceedings of the IEEE/CVF International Conference on Computer Vision (ICCV)* (2021), 8886–8895.
85. Motiian, S., Piccirilli, M., Adjeroh, D. A. & Doretto, G. *Unified Deep Supervised Domain Adaptation and Generalization in IEEE International Conference on Computer Vision (ICCV)* (2017).
86. Shankar, S. *et al.* *Generalizing Across Domains via Cross-Gradient Training in International Conference on Learning Representations* (2018), 12.
87. Muandet, K., Fukumizu, K., Sriperumbudur, B. & Schölkopf, B. *Kernel Mean Embedding of Distributions: A Review and Beyond* arXiv: 1605.09522 (2016).
88. Vicar, T., Hejc, J., Novotna, P., Ronzhina, M. & Janousek, O. *ECG Abnormalities Recognition Using Convolutional Network With Global Skip Connections and Custom Loss Function in 2020 Computing in Cardiology* (2020), 1–4.
89. Huang, G., Liu, Z. & Weinberger, K. Q. *Densely Connected Convolutional Networks. 2017 IEEE Conf. Comput. Vis. Pattern Recognit. CVPR*, 2261–2269 (2017).
90. He, K., Zhang, X., Ren, S. & Sun, J. *Deep Residual Learning for Image Recognition in 2016 IEEE Conference on Computer Vision and Pattern Recognition (CVPR)* (2016), 770–778.

## A Appendix

### A.1 Proof for Proposition 3.1

*Proof.* Suppose we have a representation,

$$\mu_{\mathbb{P}} = \sum_{i=1}^M \beta_i \mu_{V_i} \quad \langle \mu_{V_i}, \mu_{V_j} \rangle_{\mathcal{H}} = 0 \quad \forall i \neq j, \quad (\text{A.1})$$

i.e.  $\{\mu_{V_1}, \dots, \mu_{V_m}\}$  are pairwise orthogonal. We want to minimize the MMD by minimizing

$$\|\mu_{\mathbb{P}} - \sum_{i=1}^M \beta_i \mu_{V_i}\|_{\mathcal{H}}^2 = \underbrace{\langle \mu_{\mathbb{P}}, \mu_{\mathbb{P}} \rangle_{\mathcal{H}}}_{\|\mu_{\mathbb{P}}\|_{\mathcal{H}}^2} - 2 \langle \mu_{\mathbb{P}}, \sum_{i=1}^M \beta_i \mu_{V_i} \rangle_{\mathcal{H}} + \langle \sum_{i=1}^M \beta_i \mu_{V_i}, \sum_{j=1}^M \beta_j \mu_{V_j} \rangle_{\mathcal{H}} \quad (\text{A.2})$$

$$= \|\mu_{\mathbb{P}}\|_{\mathcal{H}}^2 - 2 \sum_{i=1}^M \beta_i \langle \mu_{\mathbb{P}}, \mu_{V_i} \rangle_{\mathcal{H}} + \sum_{i=1}^M \sum_{j=1}^M \beta_i \beta_j \underbrace{\langle \mu_{V_i}, \mu_{V_j} \rangle_{\mathcal{H}}}_{\delta_{ij} \langle \mu_{V_i}, \mu_{V_j} \rangle_{\mathcal{H}}} \quad (\text{A.3})$$

$$= \|\mu_{\mathbb{P}}\|_{\mathcal{H}}^2 - 2 \sum_{i=1}^M \beta_i \langle \mu_{\mathbb{P}}, \mu_{V_i} \rangle_{\mathcal{H}} + \sum_{j=1}^M \beta_j^2 \|\mu_{V_j}\|_{\mathcal{H}}^2. \quad (\text{A.4})$$

By defining

$$\Phi(\beta) := \|\mu_{\mathbb{P}} - \sum_{i=1}^M \beta_i \mu_{V_i}\|_{\mathcal{H}}^2, \quad (\text{A.5})$$

we can simply find the optimal  $\beta_i$  by using the partial derivative

$$\frac{\partial \Phi}{\partial \beta_i} = -2 \langle \mu_{\mathbb{P}}, \mu_{V_i} \rangle_{\mathcal{H}} + 2 \beta_i \|\mu_{V_i}\|_{\mathcal{H}}^2 \stackrel{!}{=} 0 \quad (\text{A.3})$$

$$\Leftrightarrow \beta_i \|\mu_{V_i}\|_{\mathcal{H}}^2 = \langle \mu_{\mathbb{P}}, \mu_{V_i} \rangle_{\mathcal{H}} \quad (\text{A.4})$$

$$\Leftrightarrow \beta_i^* = \frac{\langle \mu_{\mathbb{P}}, \mu_{V_i} \rangle_{\mathcal{H}}}{\|\mu_{V_i}\|_{\mathcal{H}}^2}. \quad (\text{A.5})$$

Please note that the function  $\Phi$  is convex. □

### A.2 Detailed View of the Regularization Term $\Omega_D^{OLS}$

First, consider the following single term  $\|\phi(x_i) - \sum_{j=1}^M \beta_{ij} \mu_{V_j}\|_{\mathcal{H}}^2$  that can be expressed as

$$\|\phi(x_i) - \sum_{j=1}^M \beta_{ij} \mu_{V_j}\|_{\mathcal{H}}^2 = \underbrace{\|\phi(x_i)\|_{\mathcal{H}}^2}_{(1)} - 2 \underbrace{\langle \phi(x_i), \sum_{j=1}^M \beta_{ij} \mu_{V_j} \rangle_{\mathcal{H}}}_{(2)} + \underbrace{\|\sum_{j=1}^M \beta_{ij} \mu_{V_j}\|_{\mathcal{H}}^2}_{(3)}. \quad (\text{A.6})$$

**Ad (1):**

We begin with Term (1) and write  $\|\phi(x_i)\|_{\mathcal{H}}^2$  as  $\|\phi(x_i)\|_{\mathcal{H}}^2 = \langle \phi(x_i), \phi(x_i) \rangle_{\mathcal{H}} = k(x_i, x_i)$ . We could evaluate this term using the kernel function  $k$  for each data point in the batch  $b$ . However, since this term does not depend on the elementary domains  $\{V_1, \dots, V_M\}$ , it is unnecessary to compute this value to minimize the penalty. Thus, we obtain a similar result by minimizing the penalty without considering  $\|\phi(x_i)\|_{\mathcal{H}}^2$  in the regularization.

**Ad (2):**

Term (2) can be expressed as

$$\langle \phi(x_i), \sum_{j=1}^M \beta_{ij} \mu_{V_j} \rangle_{\mathcal{H}} = \sum_{j=1}^M \beta_{ij} \langle \phi(x_i), \mu_{V_j} \rangle_{\mathcal{H}} \quad (\text{A.7})$$

Implementation-wise, the evaluation of this term requires the calculation of the inner product  $\langle \phi(x_i), \mu_{V_j} \rangle_{\mathcal{H}}$ . Since our CS and projection-based methods involve this inner product to determine the coefficients  $\beta_{ij}$ , we pre-compute the inner product  $\langle \phi(x_i), \mu_{V_j} \rangle_{\mathcal{H}}$  once for a mini-batch and store these information during training to avoid multiple calculations of the same term.

Moreover, the projection-based method does not apply softmax and has a linear form. Therefore, the term (2) can be simplified even further:

$$\langle \phi(x_i), \sum_{j=1}^M \beta_{ij} \mu_{V_j} \rangle_{\mathcal{H}} = \sum_{j=1}^M \beta_{ij} \langle \phi(x_i), \mu_{V_j} \rangle_{\mathcal{H}} \quad (\text{A.8})$$

$$= \sum_{j=1}^M \frac{\langle \phi(x_i), \mu_{V_j} \rangle_{\mathcal{H}}}{\|\mu_{V_j}\|_{\mathcal{H}}^2} \langle \phi(x_i), \mu_{V_j} \rangle_{\mathcal{H}} \quad (\text{A.9})$$

$$= \sum_{j=1}^M \frac{\langle \phi(x_i), \mu_{V_j} \rangle_{\mathcal{H}}^2}{\|\mu_{V_j}\|_{\mathcal{H}}^2}. \quad (\text{A.10})$$

**Ad (3):**

Last, we express the term (3) as follows

$$\left\| \sum_{j=1}^M \beta_{ij} \mu_{V_j} \right\|_{\mathcal{H}}^2 = \sum_{j=1}^M \sum_{k=1}^M \beta_{ij} \beta_{ik} \langle \mu_{V_j}, \mu_{V_k} \rangle_{\mathcal{H}}, \quad (\text{A.11})$$

and calculate the inner product of the domains  $\langle \mu_{V_j}, \mu_{V_k} \rangle_{\mathcal{H}}$  by

$$\langle \mu_{V_j}, \mu_{V_k} \rangle_{\mathcal{H}} = \frac{1}{N^2} \sum_{l=1}^N \sum_{m=1}^N \langle \phi(v_j^l), \phi(v_k^m) \rangle_{\mathcal{H}} \quad (\text{A.12})$$

$$= \frac{1}{N^2} \sum_{l=1}^N \sum_{m=1}^N k(v_j^l, v_k^m) =: K_{jk}, \quad (\text{A.13})$$

where  $N$  represents the number of vectors per domain basis. Note that this term does not depend on the input data  $x_i$  and, hence, matrix  $K_{jk}$  can be calculated once at the beginning of the optimization step and stored to be re-used for all the data point of a batch.

Combining Equation A.11 and Equation A.13 yields

$$\left\| \sum_{j=1}^M \beta_{ij} \mu_{V_j} \right\|_{\mathcal{H}}^2 = \sum_{j=1}^M \sum_{k=1}^M \beta_{ij} \beta_{ik} \langle \mu_{V_j}, \mu_{V_k} \rangle_{\mathcal{H}} \quad (\text{A.14})$$

$$= \frac{1}{N^2} \sum_{j=1}^M \sum_{k=1}^M \beta_{ij} \beta_{ik} \sum_{l=1}^N \sum_{m=1}^N k(v_j^l, v_k^m) \quad (\text{A.15})$$

$$= \sum_{j=1}^M \sum_{k=1}^M \beta_{ij} \beta_{ik} K_{jk} \quad (\text{A.16})$$

$$= \beta_i^T K_{jk} \beta_i. \quad (\text{A.17})$$

As a final step, we use the results for Term (1), (2), and (3) to obtain the desired regularization term



$$\Omega_D^{OLS} = \frac{1}{b} \sum_{i=1}^b \left( \left\| \phi(x_i) - \sum_{j=1}^M \beta_{ij} \mu_{V_j} \right\|_{\mathcal{H}}^2 \right) \quad (\text{A.18})$$

$$= \frac{1}{b} \sum_{i=1}^b \left( \left\| \phi(x_i) \right\|_{\mathcal{H}}^2 - 2 \langle \phi(x_i), \sum_{j=1}^M \beta_{ij} \mu_{V_j} \rangle_{\mathcal{H}} + \left\| \sum_{j=1}^M \beta_{ij} \mu_{V_j} \right\|_{\mathcal{H}}^2 \right). \quad (\text{A.19})$$

As mentioned above,  $\|\phi(x_i)\|_{\mathcal{H}}^2$  is independent from the elementary domains, and, thus a constant in the regularization. Hence, we can exclude this term, which avoids additional computational effort.

### A.3 Visualization of DG Layer

Figure 3 depicts the layout of our DG layer.

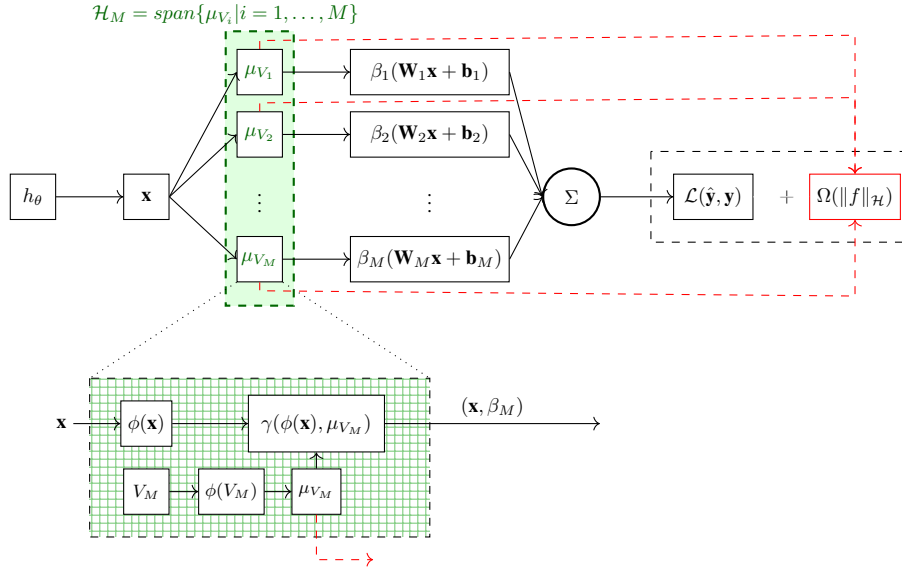


Figure 3: Domain generalization (DG) layer.

### A.4 Experiments

In this section, we provide a detailed description of the DG experiment presented in Section 5. All experiments are implemented using TensorFlow 2.4.1 and TensorFlow Probability 0.12.1. The code is publicly available on GitHub at <https://github.com/im-ethz/pub-gdu4dg>. Overall, our experiments aim to show the validity of the invariant elementary distribution (I.E.D.) assumption and the Gated Domain Units (GDUs). For this purpose, we designed the experiments as simple as possible.

#### A.4.1 Digits Experiment

Our experiment setup is closely related to Zhao *et al.* [3], Peng *et al.* [73], Feng *et al.* [74], and Zhang *et al.* [75]. Each dataset, except USPS, is split into training and test sets of 25,000 and 9,000 images, respectively. For USPS, we take the whole dataset for the experiment since it contains only 9,298 images<sup>3</sup>. Our experimental setup regarding datasets, data loader, and FE are based on existing work [73, 74]. The structure of the FE is summarized in Table 5 and the subsequent learning machine is a dense layer.

In the Empirical Risk Minimization (ERM) single experiment, we add a dense layer with 10 outputs (activation= $\tanh$ ) as a classifier to the FE. In the Empirical Risk Minimization (ERM) ensemble

<sup>3</sup>We used the digits data from <https://github.com/FengHZ/KD3A> [last accessed on 2022-05-17, available under MIT License.] published in [74].

Table 5: Feature Extractor used for the Digits Experiment

FEATURE EXTRACTOR	
LAYER TYPE	OUTPUT SHAPE
2D-CONVOLUTIONAL LAYER	(32, 32, 64)
BATCH NORMALIZATION	(32, 32, 64)
MAXPOOLING 2D	(16, 16, 64)
2D-CONVOLUTIONAL LAYER	(16, 16, 64)
BATCH NORMALIZATION	(16, 16, 64)
MAXPOOLING 2D	(8, 8, 64)
2D-CONVOLUTIONAL LAYER	(8, 8, 128)
BATCH NORMALIZATION	(8, 8, 128)
MAXPOOLING 2D	(4, 4, 128)
FLATTEN	(2048)
DENSE LAYER	(3072)
BATCH NORMALIZATION	(3072)
DROPOUT	(3072)
BATCH NORMALIZATION	(2048)
DENSE LAYER	(2048)

experiment, we add  $M$  classification heads (a dense layers with 10 outputs and  $\tanh$  activation each) to the FE and average their output for the final prediction. This sets a baseline for our DG layer to show performance gain against the ERM model with the same number of learning machines. For the DG layer, we considered two modes of model training: fine tuning (FT) and end-to-end training (E2E). In FT scenario, we first pre-train the FE in the ERM single fashion. Then, we extract features using the pre-trained model and pass them to the DG layer for training the latter. For the E2E training, however, the whole model including the FE and DG layer is trained jointly from the very beginning.

For training, we resorted to the Adam optimizer with a learning rate of 0.001. We used early stopping and selected the best model weights according to the validation accuracy. For the validation data, we used the combined test splits only of the respective source datasets. The batch size was set to 512. Although the DG layer requires more computation resources than the ERM models, all digits experiments were conducted on a single GPU (NVIDIA GeForce RTX 3090).

Table 6: Parameters for DG Layer in Digits and Digit-DG Experiments for the Fine Tuning (FT) and End-to-end training (E2E) Settings. In case of Projection, we chose the spectral restricted isometry property (SRIP) as the orthogonal regularization  $\Omega_D^\perp$ .

EXPERIMENT		M	N	$\lambda_{L_1}$	$\lambda_{OLS}$	$\lambda_{ORTH}$	$\sigma$	$\kappa$
FT	CS	5	10	$1e^{-3}$	$1e^{-3}$	-	$\hat{\sigma}$	2
	MMD	5	10	$1e^{-3}$	$1e^{-3}$	-	$\hat{\sigma}$	2
	PROJECTION	5	10	$1e^{-3}$	$1e^{-3}$	$1e^{-8}$	$\hat{\sigma}$	-
E2E	CS	5	10	$1e^{-3}$	$1e^{-3}$	-	7.5	2
	MMD	5	10	$1e^{-3}$	$1e^{-3}$	-	7.5	2
	PROJECTION	5	10	$1e^{-3}$	$1e^{-3}$	$1e^{-8}$	7.5	-

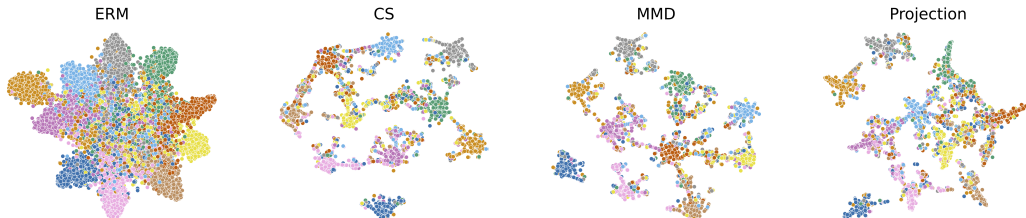


Figure 4: Visualization of t-SNE Embedding on unseen Synthetic Digits Dataset. Colors encode true label.

**Digit-DG Benchmark** In previous research, the aforementioned digits data is not only used for domain adaptation (DA), but also for domain generalization (DG) methods. For the latter, Zhou *et al.* [83] and Li *et al.* [84] introduced Digit-DG dataset and the evaluation protocol to benchmark seven DG methods and ERM<sup>4</sup>. Unlike the Digits experiment described above, Digit-DG dataset from Zhou *et al.* [83] and Li *et al.* [84] consists of only four datasets (without USPS) and a different FE summarized in Table 7. Therefore, we follow their instructions to conduct a fair comparison and ensure reproducibility. For the hyper-parameters, however, we kept the same values that we used for the Digits experiment, see Table 6.

Table 7: Feature Extractor used for the Digit-DG Benchmark Experiment

FEATURE EXTRACTOR	
LAYER TYPE	OUTPUT SHAPE
2D-CONVOLUTIONAL LAYER	(32, 32, 64)
MAXPOOLING 2D	(16, 16, 64)
2D-CONVOLUTIONAL LAYER	(16, 16, 64)
MAXPOOLING 2D	(8, 8, 64)
2D-CONVOLUTIONAL LAYER	(8, 8, 64)
MAXPOOLING 2D	(4, 4, 128)
2D-CONVOLUTIONAL LAYER	(8, 8, 64)
MAXPOOLING 2D	(4, 4, 128)
2D-CONVOLUTIONAL LAYER	(4, 4, 64)
MAXPOOLING 2D	(2, 2, 64)
FLATTEN	(256)

As a first method, we consider the CCSA (Classification and Contrastive Semantic Alignment) method, which learns a domain-invariant representation by utilizing the CCSA loss [85]. Second, MMD-AAE (Maximum Mean Discrepancy-based Adversarial Autoencoders) extends adversarial autoencoders by a maximum mean discrepancy regularization to learn a domain-invariant feature representation [12]. CrossGrad (Cross-Gradient) augments data by perturbing the input space using the cross-gradients of a label and domain predictor [86]. Another augmentation-based DG method is L2A-OT (Learning to Augment by Optimal Transport) [83]. Specifically, a data generator trained to maximize the optimal transport distance between source and pseudo domains, is used to augment the source data. All aforementioned methods rely on the availability of domain information such as domain labels. To benchmark our layer to a method for DG without domain information, we resort to the JiGen (Jigsaw puzzle based Generalization) method [68]. JiGen introduces an auxiliary loss for solving jigsaw task during training. Further, we use the adaptive and non-adaptive stochastic feature augmentation (SFA-S and SFA-A, respectively) method proposed by Li *et al.* [84]. In principle, both method augment the latent feature embedding of a FE using random noise.

Our results are summarized in Table 8. As noted by Li *et al.* [84], it is challenging to outperform augmentation-based DG methods. In addition, SFA-A and SF-S are computationally light (i.e., only adding random noise to the feature embedding) and do not require domain information [84]. Nevertheless, our layer outperforms even the strongest baselines in all DG tasks without requiring domain information. However, the disadvantage of our layer is the additional computational overhead, which we analyze in the Appendix A.4.7.

#### A.4.2 Heuristics for main parameter of DG layer

From a practical perspective, our layer requires choosing two main hyper-parameters: the number of elementary domains  $M$  and since we use the characteristics Gaussian kernel the corresponding parameter  $\sigma$ . The parameter  $M$  determines the size of the ensemble of learning machines and, thus, for deep learning models, their overall network size. As a heuristic to choose  $M$ , we suggest to cluster the output of a pre-trained FE. In the following, we provide an example. We pre-trained the FE for the test domain  $MNIST-M$  and pass the source data through this FE, which we cluster with the k-means algorithm. Subsequently, we analyse three different metrics (Calinski Harabasz score, Davies Bouldin score, and Silhouette score) to select the optimal number of clusters as the basis to

<sup>4</sup>Results were reported by Zhou *et al.* [83] and Li *et al.* [84]. Of note, both authors did not report the standard deviation on their results.

Table 8: Results of the Digits-DG experiment. All experiments were repeated ten times. Methods are classified into augmentation-based (A) and non-augmentation-based (B) as well as DG with ( $\times$ ) and without (W/O,  $\checkmark$ ) domain information according to Li *et al.* [84]. Best results according to the mean accuracy are highlighted in **bold**.

	MNIST	MNIST-M	SVHN	SYN	CATEGORIE	W/O DOMAIN INFORMATION	
<i>ERM</i>	95.8	58.8	61.7	78.6	B	$\checkmark$	
<i>CCSA</i> [85]	95.2	58.2	65.5	79.1	B	$\times$	
<i>MMD-AAE</i> [12]	96.5	58.4	65.0	78.4	B	$\times$	
<i>CrossGrad</i> [86]	96.7	61.1	65.3	80.2	A	$\times$	
<i>L2A-OT</i> [83]	96.7	63.9	68.6	83.2	A	$\times$	
<i>SFA-S</i> [84]	96.7	66.3	68.8	85.1	A	$\checkmark$	
<i>SFA-A</i> [84]	96.5	66.5	70.3	85.0	A	$\checkmark$	
<i>JiGen</i> [68]	96.5	61.4	63.7	74.0	B	$\checkmark$	
<i>Gated Domain Units (GDUs)</i>							
	CS	97.5	68.9	74.0	85.5	B	$\checkmark$
<b>FT</b>	MMD	97.6	69.0	74.2	84.3	B	$\checkmark$
	PROJECTION	97.7	69.1	74.1	86.1	B	$\checkmark$
	CS	97.6	69.4	<b>75.9</b>	<b>86.5</b>	B	$\checkmark$
<b>E2E</b>	MMD	97.6	<b>69.5</b>	75.6	<b>86.5</b>	B	$\checkmark$
	PROJECTION	<b>97.8</b>	66.7	73.4	84.0	B	$\checkmark$

choose  $M$ . All scores yielded an accordance between four to five clusters. Therefore, we set  $M$  to five and observed in Table 2 in Section 5 strong results in the generalizing to the unseen test domain *MNIST-M*.

As for the parameter  $\sigma$ , we resort to the median heuristic proposed in [87] that is  $\sigma^2 = \text{median}\{\|\tilde{x}_i - \tilde{x}_j\|^2 : i, j = 1, \dots, n\}$ . While both heuristics require a pre-trained FE, cross-validation can act as a reasonable alternative.

The hyper-parameters relevant for the DG layer are summarized in Table 6. In the FT setting, we applied the median heuristics presented above to estimate  $\sigma$  of the Gaussian kernel function, where the estimator is denoted as  $\hat{\sigma}$ . Since median heuristic is not applicable for the E2E scenario,  $\sigma$  was fixed to 7.5 for E2E.

Note that our approach to choose the relevant parameters was kept very general to show the feasibility of the I.E.D. assumption and the generalization ability of GDUs and, most importantly, to provide easy-to-reproduce results. During training, additional epoch metrics can be subscribed using our custom *DG layer callback*, which may help to choose the model parameters. Furthermore, we observed that the elementary domains become naturally orthogonal during the experiments, and thus, we set  $\lambda_{ORTH}$  relatively small. Since the orthogonal regularization puts additional computational burden, one could omit this term completely to speed up training.

### A.4.3 Ablation Study

We chose the Digits dataset to conduct an ablation study, which is organized as follows: (1) ablation of the regularization terms presented in Section 3, (2) effect of the orthogonal regularization for projection-based generalization, and (3) visualization of learned elementary domains.

As a reminder, we introduced the regularization to be dependent on the form of generalization (i.e., domain similarity measures or projection-based generalization in Section 3). For the domain similarity measure case, the regularization is

$$\Omega_D(\|g\|_{\mathcal{H}}) = \lambda_{OLS}\Omega_D^{OLS}(\|g\|_{\mathcal{H}}) + \lambda_{L_1}\Omega_D^{L_1}(\|g\|), \quad (\text{A.20})$$

where  $\lambda_{OLS}, \lambda_{L_1} \geq 0$ . In the case of projection, the regularization is given by

$$\Omega_D(\|g\|_{\mathcal{H}}) = \lambda_{OLS}\Omega_D^{OLS}(\|g\|_{\mathcal{H}}) + \lambda_{ORTH}\Omega_D^{\perp}(\|g\|_{\mathcal{H}}) \quad (\text{A.21})$$

with  $\lambda_{OLS}, \lambda_{ORTH} \geq 0$ . Although one can additionally choose the sparse regularization in projection-based generalization, we set the focus in the ablation study on the two main regularization terms that are the OLS and orthogonal regularization. For (1) we vary in Equation A.20 and Equation A.21 the corresponding weights  $\lambda_1$  and  $\lambda_2$  in the interval of  $[0; 0.1]$  and display the mean classification

accuracy for the most challenging classification task of MNSIT-M in the form of a heatmap. In Figures 5-7, we see that the classification accuracy remains on an overall similar level which indicates that the DG layer is not very sensitive to the hyper-parameter change for MNIST-M as the test domain. Nevertheless, we observe that ablating the regularization terms by setting the corresponding weights to zero decreases the classification results and the peaks in performance occur when the regularization is included during training of the DG layer.

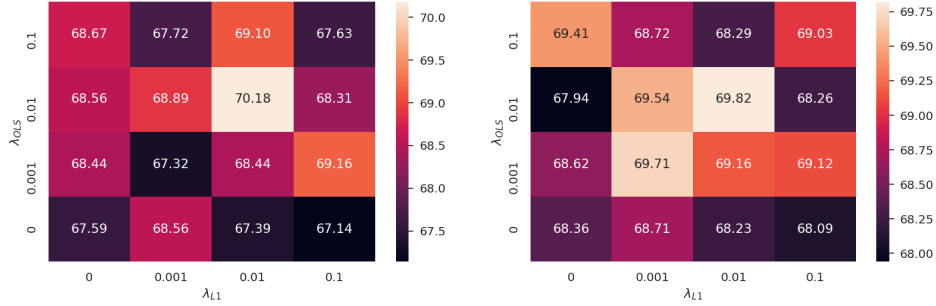


Figure 5: Classification results for varying  $\lambda_{L_1}$  and  $\lambda_{OLS}$  in the interval of  $[0; 0.1]$  for FT (left) and E2E (right) MMD on MNIST-M.

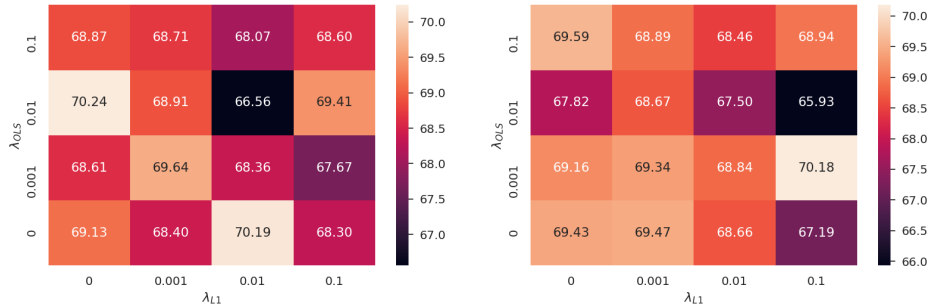


Figure 6: Classification results for varying  $\lambda_{L_1}$  and  $\lambda_{OLS}$  in the interval of  $[0; 0.1]$  for FT (left) and E2E (right) CS on MNIST-M.

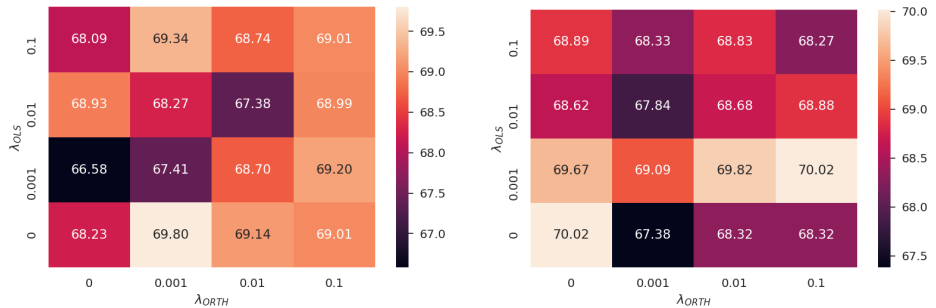


Figure 7: Classification results for varying  $\lambda_{ORTH}$  and  $\lambda_{OLS}$  in the interval of  $[0; 0.1]$  for FT (left) and E2E (right) Projection on MNIST-M.

Applying the DG layer comes with additional overhead, especially the regularization that ensures the orthogonality of the elementary domain bases. This additional effort raises a question whether ensuring the theoretical assumptions outweigh the much higher computational effort. Thus, in a second step, we analyze how the orthogonal regularization affects the orthogonality of the elementary domain bases (i.e., spectral restricted isometry property (SRIP) value) and the loss function (i.e., categorical cross-entropy).

In Figure 9, we depict the mean and standard deviation of the SRIP value and loss over five runs for 40 epochs. The SRIP value can be tracked during training with the DG layer’s callback functionalities. First, we observe that the elementary domains are almost orthogonal when initialized. Training the layer leads in the first epochs to a decrease in orthogonality. This initial decrease happens because cross-entropy has a stronger influence on the optimization than regularization in the first epochs. After five epochs, the cross-entropy decrease to a threshold when the regularization becomes more effective and the orthogonality of the elementary domain bases increases again. In Figure 9, we also observe that ablating the orthogonal regularization, while leading to better orthogonality of the domains, does not significantly affect the overall cross-entropy during training.

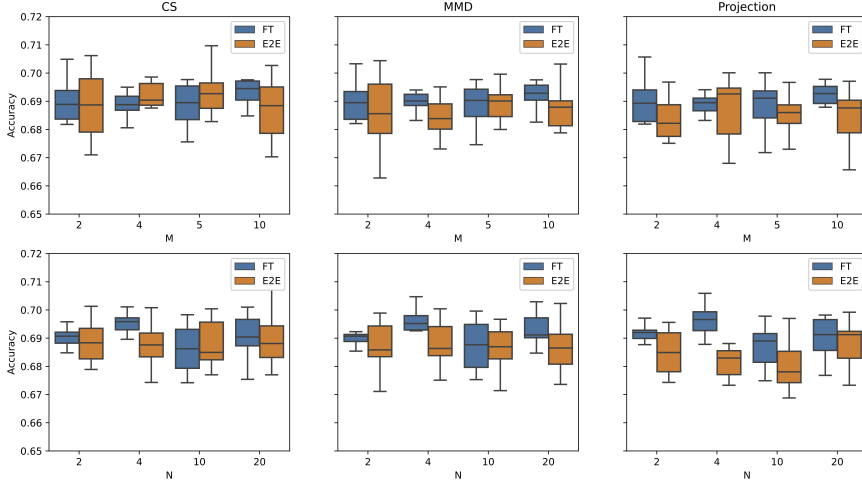


Figure 8: Mean and standard deviation of classification accuracy over 10 runs for varying number of elementary domains ( $M$ , upper panel) and varying number of vector for each domain basis ( $N$ , lower panel) for MNIST-M dataset.

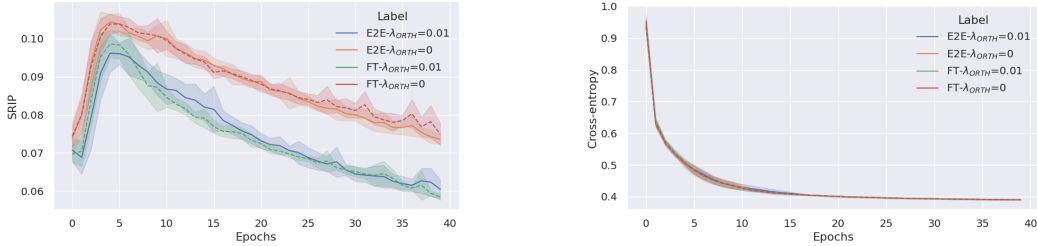


Figure 9: Effect of omitting the orthogonal regularization term  $\Omega_D^\perp$ . spectral restricted isometry property (SRIP) (left) and categorical cross-entropy (right) with and without orthogonal regularization and their evolution during training for MNSIT-M dataset. The mean and standard deviation presented for End-to-end (E2E) and Fine-tuning (FT) training scenarios are calculated over 10 runs.

#### A.4.4 Interpretation of the Elementary Domains

We analyze the learned elementary domains in the digits experiment based on two visualizations, and choose the maximum mean discrepancy (MMD) as the similarity measure and *MNIST-M* as the test domain. The first visualization depicts the MMD between the datasets (i.e., *MNIST*, *MNIST-M*, *SVHN*, *USPS*, and *Synthetic Digits (SYN)*) and the learned elementary domains (i.e.,  $V_1 - V_5$ ) as a heatmap (see Figure 10 (left)). The heatmap indicates that the source and test domains are close to one another in terms of the MMD. Hence, we expect that their closeness reflects in the learning of the elementary domains. In other words, we expect that each elementary domains contributes similarly to

Table 9: ECG Data Sources Details.

DATASET	NUMBER OF SAMPLES	ECG LENGTH [SEC]	FREQUENCY	COUNTRY
CPSC	6,877	6 TO 60	500 HZ	CHINA
CPSC-EXTRA	3,453	6 TO 60	500 HZ	CHINA
INCART	75	1,800	257 HZ	RUSSIA
PTB	549	UP TO 120	1,000 HZ	GERMANY
PTB-XL	21,837	10	500 HZ	GERMANY
G12EC	10,344	10	500 HZ	USA

the source and test domains (i.e., the coefficients  $\beta$  are similar for each of these domains). In Section 3.1, we derive the coefficients by applying a kernel softmax function to the negative MMD distances. Since the MMD distances between the source / test domains and the elementary domains are similar, the coefficients will be similar too. We conclude that the learned elementary domains represent the same distributional characteristics that existed among the source and test domains.

In the second visualisation, we show the t-SNE (t-distributed stochastic neighbor embedding) of the feature extractor output for each source and test domain alongside the elementary domains in Figure 10 (right). First, we observe that the learned elementary domain bases form distinctive clusters. We see these clusters as a validation of our hypothesis that each GDU learns to mimic samples generated from a corresponding elementary distribution as pointed out in Section 2.2. However, we can not answer whether and where these elementary distributions occur in the real world. Moreover, these elementary distributions yet lack interpretability.

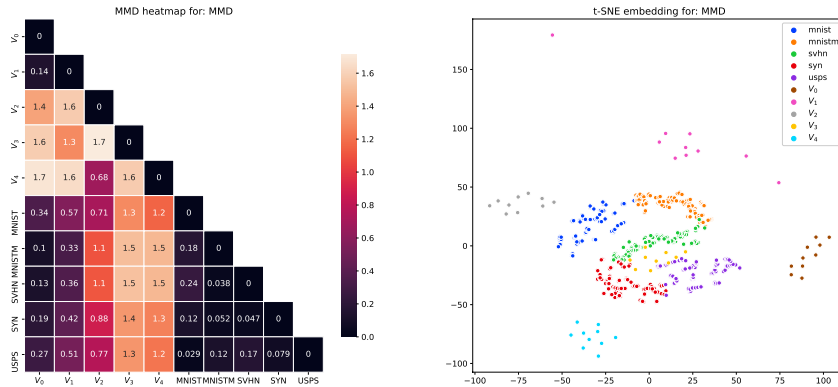


Figure 10: MMD heatmap (left) and t-SNE embedding (right) for the test domain MNIST-M.

### A.4.5 ECG Experiment

We adopted the task of multi-label binary classification of 12-lead electrocardiogram (ECG) signals combined from 6 different sources introduced in the *PhysioNet/Computing in Cardiology Challenge 2020*<sup>5</sup> [76–78]. Each ECG recordings is annotated with 24 binary labels indicating whether or not a certain cardiac abnormality is present. The data is aggregated from 6 different databases and contains 43,101 recordings sampled with various sampling frequencies, number of subjects, and lengths. Table 9 summarizes most important details about the data sources for this experiment.

According to the original challenge score, we measure the performance in terms of the generalized Intersection-over-Union (IoU) score where partial credit is assigned to misdiagnoses that result in similar treatments or outcomes. The score is defined as

$$score := \frac{y^T \cdot W \cdot \hat{y}}{y \cup \hat{y}}, \tag{A.22}$$

<sup>5</sup><https://physionetchallenges.org/2020/> [last accessed on 2021-03-10, available under Creative Commons Attribution 4.0 International Public License].

where  $y, \hat{y} \in \{0, 1\}^{24}$  represent actual labels and predicted labels and  $W$  stands for the partial credit-assignment matrix provided as a part of the challenge description. Note that in case of identity matrix  $W$  the score is exactly the Intersection-over-Union (IoU) score. The score is then adjusted for a solution  $y_{majority}$ , which always predicts the normal/majority class, and is moreover normalized for the perfect solution  $y$ . Therefore, the final score can have negative values and the best possible score of 1 and is formalized as

$$adjusted\ score := \frac{score(y, \hat{y}) - score(y, y_{majority})}{score(y, y) - score(y, y_{majority})}. \quad (\text{A.23})$$

As a pre-processing step, we down-sampled all the signals to 125 Hz and applied Z-score, random amplification and random stretching according to Vicar *et al.* [88]. For that we partially adopted the code provided by the authors<sup>6</sup>. Additionally, we cropped each signal to its first 15,000 points if the signal was too long (mostly applied to *INCART* database). Each dataset was randomly split into train and validation parts with 3:1 ratio. During each experiment, we used the train splits of 5 databases for training and utilized the validation splits of the training databases for early stopping. The hold-out 6-th database was used for inference and testing only.

Table 10 describes the architecture of FE used for the task. Since the provided ECG recordings have different lengths, we used TensorFlow padded batching, which is padding all the recordings in a batch to the length of the longest sequence in the batch. Therefore, input from different batches can have different lengths so the spatial dimensions of the 1D-Convolutional layers are not predefined and are presented as \*.

Table 10: Feature Extraction Architecture used for the ECG Experiment is an adapted Version of LeNet Architecture for 1D input Signals. Note that ECG recordings have variable lengths, therefore, the spatial dimension is not defined and denoted as \*.

FEATURE EXTRACTOR	
LAYER TYPE	OUTPUT SHAPE
1D-CONVOLUTIONAL LAYER (KERNEL SIZE=3, ACTIVATION= <i>relu</i> )	(* , 32)
BATCH NORMALIZATION	(* , 32)
MAXPOOLING 1D (POOL SIZE=2, STRIDES=2)	(* , 32)
1D-CONVOLUTIONAL LAYER (KERNEL SIZE=2, ACTIVATION= <i>relu</i> )	(* , 64)
BATCH NORMALIZATION	(* , 64)
GLOBAL AVERAGE POOLING 1D	(64)
DENSE LAYER (ACTIVATION= <i>relu</i> )	(100)
DENSE LAYER (ACTIVATION= <i>relu</i> )	(100)

We used the Adam optimizer to optimize weighted binary cross-entropy loss defined as  $-(w_{pos} \cdot y \cdot \log \hat{y}) + (1 - y) \cdot \log (1 - \hat{y})$ . Positive weights  $w_{pos}$  are defined per class based on the training split data inversely proportional to the frequency of positive labels for each class. A learning rate was initially set to 0.001 and during the training reduced by the factor of 0.2 if the training loss was not improving for 10 epochs. We also applied early stopping and restored model weights to the best model according to the validation accuracy after the training end. Since each input samples for this experiment have a larger size than the previous one, we decreased the batch size to 64. Each ECG experiment was performed on a single GPU (Nvidia GTX 1080 Ti). The parameters relevant for the DG layer are summarized in Table 11. We have to emphasize that we did not perform extensive hyper-parameter tuning since our goal was to show the feasibility of the I.E.D. assumption and GDUs while keeping the experiments reproducible.

#### A.4.6 WILDS Benchmarking Experiments

For comparison of our approach and benchmarking, we followed the standard procedure of WILDS experiments, described in Koh *et al.* [79]. Below, we shortly outline the settings for each of the datasets we used together with any modification we had to make.

As a technical note, all WILDS experiments have been implemented in Pytorch (version  $\geq 1.7.0$ ). Based on the specifications made in Koh *et al.* [79] and their code published on <https://github.com/p-lambda/wilds> [last accessed on 2022-05-17, available under MIT License], we reproduced

<sup>6</sup><https://github.com/tomasvicar/BUTTeam> [last accessed on 2022-05-17, available under BSD 2-Clause License].



Table 11: Parameters for DG Layer in ECG experiments for the Fine Tuning (FT) and End-to-end training (E2E) Settings.

EXPERIMENT		M	N	$\lambda_{L_1}$	$\lambda_{OLS}$	$\lambda_{ORTH}$	$\sigma$	$\kappa$
FT	CS	10	10	$1e^{-3}$	$1e^{-3}$	-	5.5	2
	MMD	10	10	$1e^{-3}$	$1e^{-3}$	-	5.5	2
	PROJECTION	10	10	$1e^{-3}$	$1e^{-3}$	$1e^{-6}$	5.5	-
E2E	CS	10	10	$1e^{-3}$	$1e^{-3}$	-	5.5	2
	MMD	10	10	$1e^{-3}$	$1e^{-3}$	-	5.5	2
	PROJECTION	10	10	$1e^{-3}$	$1e^{-3}$	$1e^{-6}$	5.5	-

their results in TensorFlow to make the baseline results comparable to the ones achieved by our DG layer. Due to the high workload to replicate all methods, we have focused on the ERM assumption, which is considered as one of the strongest baselines in their experiments.

**Camelyon17** In medical applications, the goal is to apply models trained on a comparatively small set of hospitals to a larger number of hospitals. For this application, we study images of tissue slides under a microscope to determine whether a patient has cancer or not. Shifts in patient populations, slide staining, and image acquisition can impede model accuracy in previously unseen hospitals. Camelyon17 comprises images of tissue patches from five different hospitals. While the first three hospitals are the source domains (302,436 examples), the fourth and fifth are the validation (34,904 examples) and test domain (85,054 examples), respectively.

We deviate from the specifications made in [79] in terms of the FE. We use the FE from Peng *et al.* [73] and Feng *et al.* [74] since we observed a higher mean accuracy and faster training than with the by Koh *et al.* [79] originally proposed DenseNet-121 FE [89]. We trained the FE from scratch. Both, ERM and the DG were trained over 250 epochs with early stopping, a learning rate of 0.001, which is reduced by a factor of 0.2 if the cross-entropy loss has not improved after 10 epochs. All results were aggregated over ten runs.

**RxRx1** In biomedical research areas such as genomics or drug discovery, high-throughput screening techniques generate a vast amount of data in several batches. Because experimental designs cannot fully mitigate the effects of confounding variables like temperature, humidity, and measurements across batches, this creates heterogeneity in the observed datasets (commonly known as batch effect). The RxRx1 dataset comprises images obtained by fluorescent microscopy from 51 domains (disjoint experiments): training (40,612 images, 33 domains), validation (9,854 images, 4 domains), and test (34,432 images, 14 domains). The aim is to classify one of 1,139 genetic treatments.

We conducted the RxRx1 experiments in accordance with the specifications made in [79]. As for the FE, we, thus, used the ResNet50 pre-trained on ImageNet [90]. We trained the models using AdamW with default parameters  $\beta_1 = 0.9$  and  $\beta_2 = 0.999$  using a learning rate of  $1e-4$  and a L2-regularization with strength  $1e-5$  for 90 epochs with a batch size of 75. We scheduled the learning rate to linearly increase in the first ten epochs and then decreased it following a cosine rate. For fine-tuning the DG layer, we chose the same parameters as for the ERM. However, for the end-to-end training we chose only to increase the number of epochs to 120, while kept the rest of the specifications the same as ERM. All results were aggregated over three runs.

**iWildsCam** Wildlife camera traps offer an excellent possibility to understand and monitor biodiversity loss. However, images from different camera traps differ in illumination, color, camera angle, background, vegetation, and relative animal frequencies. We use the iWildsCam dataset consisting of 323 different camera traps positioned in different locations worldwide. In the dataset, we refer to different locations of camera traps as different domains, in particular 243 training traps (129,809 images), 32 validation traps (14,961 images), and 48 test traps (42,791 images). The objective is to classify one of 182 animal species.

Following the instructions by Koh *et al.* [79], we used again the ResNet50 pre-trained on ImageNet [90]. For ERM, we used a learning rate of  $3e-5$  and no L2-regularization. The models were trained for 12 epochs with a batch size of 16 with the Adam optimizer. In addition to the accuracy, we report

the macro F1-score to evaluate the performance on rare species (see Koh *et al.* [79] for details). All results were aggregated over three runs.

**FMoW** Analyzing satellite images with machine learning (ML) models may enable novel possibilities in tackling global sustainability and economic challenges such as population density mapping and deforestation tracking. However, satellite imagery changes over time due to human behavior (e.g., infrastructure development), and the extent of change is different in each region. The Functional Map of the World (FMoW) dataset consists of satellite images from different continents and years: training (76,863 images; between 2002–2013), validation (19,915 images; between 2013 and 2016), and test (22,108 images, between 2016–2017). The objective is to determine one of 62 building types (e.g., shopping malls) and land-use.

As instructed in Koh *et al.* [79], we used the DenseNet-121 pre-trained on ImageNet without L2-regularization. For the optimization, we use the Adam optimizer with a learning rate of  $1e-4$ , which is decayed by a factor of 0.96 per epoch. The models were trained for 50 epochs with early stopping and a batch size of 64. Additionally, we report the worst-region accuracy, which is a specific metric used for FMoW. This worst-region accuracy reports the worst accuracy across the following regions: Asia, Europe, Africa, America, and Oceania (see Koh *et al.* [79] for the details.) Again, we report the results over three runs.

Table 12: Parameters for DG Layer in WILDS experiments for the Fine Tuning (FT) and End-to-end training (E2E) Settings.

EXPERIMENT		M	N	$\lambda_{L_1}$	$\lambda_{OLS}$	$\lambda_{ORTH}$	$\sigma$	$\kappa$	
CAMELYON17	FT	CS	10	10	$1e^{-3}$	$1e^{-3}$	-	5.5	2
		MMD	10	10	$1e^{-3}$	$1e^{-3}$	-	5.5	2
		PROJECTION	10	10	-	$1e^{-3}$	$1e^{-6}$	20	-
	E2E	CS	10	10	$1e^{-3}$	$1e^{-3}$	-	5.5	2
		MMD	10	10	$1e^{-3}$	$1e^{-3}$	-	5.5	2
		PROJECTION	10	10	-	$1e^{-3}$	$1e^{-6}$	20	-
RXRX1	FT	CS	5	10	$1e^{-3}$	$1e^{-3}$	-	5.5	2
		MMD	5	10	$1e^{-3}$	$1e^{-3}$	-	5.5	2
		PROJECTION	5	10	-	$1e^{-3}$	$1e^{-6}$	20	-
	E2E	CS	5	10	$1e^{-3}$	$1e^{-3}$	-	5.5	2
		MMD	5	10	$1e^{-3}$	$1e^{-3}$	-	5.5	2
		PROJECTION	5	10	-	$1e^{-3}$	$1e^{-6}$	20	-
IWILDCAM	FT	CS	10	10	$1e^{-3}$	$1e^{-3}$	-	5.5	2
		MMD	10	10	$1e^{-3}$	$1e^{-3}$	-	5.5	2
		PROJECTION	10	10	-	$1e^{-3}$	$1e^{-6}$	20	-
	E2E	CS	10	10	$1e^{-3}$	$1e^{-3}$	-	5.5	2
		MMD	10	10	$1e^{-3}$	$1e^{-3}$	-	5.5	2
		PROJECTION	10	10	-	$1e^{-3}$	$1e^{-6}$	20	-
FMoW	FT	CS	10	10	$1e^{-3}$	$1e^{-3}$	-	5.5	2
		MMD	10	10	$1e^{-3}$	$1e^{-3}$	-	5.5	2
		PROJECTION	10	10	-	$1e^{-3}$	$1e^{-6}$	20	-
	E2E	CS	10	10	$1e^{-3}$	$1e^{-3}$	-	5.5	2
		MMD	10	10	$1e^{-3}$	$1e^{-3}$	-	5.5	2
		PROJECTION	10	10	-	$1e^{-3}$	$1e^{-6}$	20	-

#### A.4.7 Scalability

Our layer induces additional computational overhead due to the regularization and the model size that grows with the number of elementary domains. This overhead increases training time, especially for the projection-based generalization method due to an computationally expensive  $\Omega_{\frac{1}{D}}$  regularization term. To quantify this overhead, and to have a comparison with the plain ERM, we report the wall-clock time per training epoch. Note that we report only the times for end-to-end (E2E) training since in fine-tuning (FT) the weights of the feature extractor are fixed. Simply fine-tuning our layer is naturally faster than ERM and, for this reason, an unfair comparison. We summarize the wall-clock times in Table 13. Adding our layer on top of a feature extractor (e.g., ResNet50) increases the time for training.

However, in our ablation study (see Figures 7 and 9), we discuss how  $\Omega_D^\perp$  affects the performance and loss value. We observed that the loss is not affected by excluding  $\Omega_D^\perp$  and in some instances, it can be omitted without affecting the results in practice. This would make training the GDU layer faster.

Further, we achieved the improvement already with a relatively small number of elementary domains indicating that the increased complexity is not necessarily a consequence of applying the DG layer. Lastly, we leverage sparse coding to reduce the complexity of the model, and future work might additionally consider neural network pruning.

Table 13: Wall-clock Time for the WILDS Benchmarking Tasks. We compute the wall-clock time per epoch in seconds and report the mean (standard deviation) across three runs.

	CAMELYON17 DOMAINNET	RxRx1 RESNET-50	iWILDCAM RESNET-50	FMoW DENSENET-121
<b>ERM</b>	114.09 (2.70)	554.45 (67.89)	114.09 (2.70)	989.91 (113.72)
<b>CS</b>	267.29 (8.92)	640.98 (21.77)	267.29 (8.92)	1142.16 (36.98)
<b>MMD</b>	260.04 (7.74)	645.77 (13.32)	260.04 (7.74)	1115.99 (57.48)
<b>PROJECTION</b>	388.40 (9.30)	534.76 (3.75)	388.40 (9.30)	2741.54 (65.80)